8-27-2019

Multicomponent Model of Crustal Stress at Cajon Pass, Southern California with Implications for Stress Field Heterogeneity

Elliott Conley Helgans
Louisiana State University and Agricultural and Mechanical College

MULTICOMPONENT MODEL OF CRUSTAL STRESS AT CAJON PASS, SOUTHERN CALIFORNIA WITH IMPLICATIONS FOR STRESS FIELD HETEROGENEITY

A Thesis

Submitted to the Graduate Faculty of the
Louisiana State University and
Agricultural and Mechanical College
in partial fulfillment of the
requirements for the degree of
Master of Science

in

The Department of Geology and Geophysics

by
Elliott Conley Helgans
B.S., Washington and Lee University, 2016
December 2019

Acknowledgements

I thank Karen Luttrell, Patricia Persaud, and Juan Lorenzo for their valuable insight and for reviewing this work. Additionally, I appreciate Bridget Smith-Konter and Liliane Burkhard for providing estimates for stress accumulation rates along locked portions of the Cajon Pass crust. This research was supported by the Southern California Earthquake Center awards #18150 and #19070. SCEC is funded by NSF Cooperative Agreement EAR-1033462 & USGS Cooperative Agreement G12AC20038. Additional funding was provided in the form of scholarships from the New Orleans Geological Society Memorial Foundation and the Chevron Energy Leadership Academy.

Table of Contents

Abstract

Earthquake processes in plate boundary settings are chiefly controlled by the *in situ* crustal stress field. Knowledge of the relative importance of various active processes acting on a fault system is necessary to understand the mechanics of faulting. This is of extreme importance to the Cajon Pass region of southern California, which may function as an earthquake gate, imposing control on large multifault ruptures. We model the *in situ* stress field at seismogenic depth in Cajon Pass by balancing the orientation of the modern stress field inferred from earthquake focal mechanisms against the superposition of the far field tectonic driving stress, the load of topography, and the accumulation of stress on locked faults over variable loading times. We incorporate existing models for stress accumulation rate from locked faults and topography with a set of simple driving stress models, in which we treat driving stress orientations, magnitudes, as well as effective loading times on locked fault segments as free parameters. We use this model to assess relative influences of each process to the modern field observed today as well as identify any potential heterogeneity in the plate driving stress. Our results indicate that driving stress orientation may rotate clockwise (from north-northwest to north-northeast) southward across Cajon Pass and predict *in situ* differential stress magnitudes between 59 and 93 MPa in this region, consistent with previous findings. We find that the modern stress field may be most strongly influenced by heterogeneity in driving stress orientation on the scale of tens of kilometers. Despite rake angles indicating a primarily strike-slip faulting regime across Cajon Pass for our optimal model with fault segment-scale rotations in driving stress, we observe a heterogeneous distribution of maximum shear stress predicted on fault surfaces. We predict shear stress is highest, ~60 MPa, on the northern San Andreas fault, and sharply decreases to ~30 MPa at the onset of the subparallel San Jacinto fault network. The observed variations in resolved shear stress on major Cajon Pass fault surfaces indicate that heterogeneity in driving stress orientation may inhibit multifault ruptures across the region.

1. Introduction

In active plate boundary settings, improved understanding of the individual processes acting on fault systems is necessary to determine the mechanics of faulting [*Hardebeck and Hauksson*, 2001]. Consequently, it is important to determine the state of stress in the crust. In California, the San Andreas fault (SAF) represents the major active structure between the Pacific and North American plates. Stress on the SAF is presumed to result primarily from the relative motion between these two plates but is also influenced by other active tectonic processes. Observations of contrasts in stress and elastic strain accumulation in southern California suggest that principal stress orientations change across the region [*Goebel et al.*, 2015; *Hauksson*, 2015; *Yang and Hauksson*, 2013], and questions regarding the exchange between this field and active fault segments remain [*Hardebeck and Michael*, 2006]. Specifically, how does each individual process contributing to the modern stress field act on the SAF at depth? This is of extreme relevance to the Cajon Pass region, which may function as an earthquake gate, exerting control over the propagation or termination of multifault ruptures [*Lozos et al.*, 2015] (Figure 1). Dynamic rupture models at Cajon Pass are very sensitive to inputs for the background stress field, influencing strength of ground motions and total rupture extent [*Harris et al.*, 2018; *Lozos*, 2016; *Lozos et al.*, 2015]. Therefore, it is important to quantitatively describe the crustal stress field at Cajon Pass including its magnitude, orientation, and dominant scales of spatial heterogeneity, as well as inform the various geodynamic processes responsible for its development.

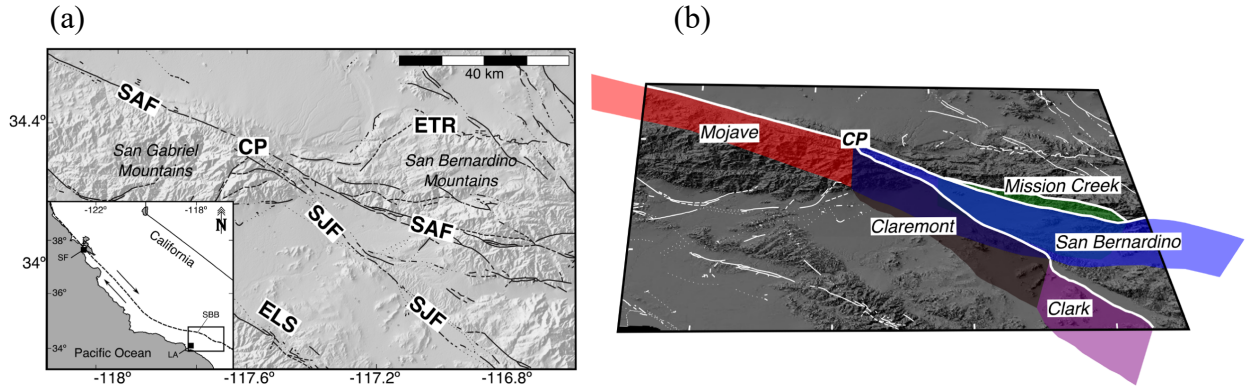

Figure 1. Regional map of Cajon Pass. (a) Surface traces of San Andreas (SAF), San Jacinto (SJF), Eastern Transverse Ranges (ETR), and Elsinore Laguna Salada (ELS) fault zones. (inset) Map showing Cajon Pass region (black box) and geometry of the San Andreas Fault (black dashed line) in California. SBB indicates the San Bernardino Bend at Cajon Pass. (b) Fault surfaces for the major San Andreas (Mojave, Mission Creek, San Bernardino) and San Jacinto (Claremont, Clark) fault segments. Segment names are adopted from *Burkhard et al.* [2018] and geometries from Southern California Earthquake Center Community Fault Model v. 5.2 [*Nicholson et al.*, 2017]. CP indicates the junction between the SAF and SJF at Cajon Pass.

The Cajon Pass region is defined by the SAF system which formed to accommodate motion on the transform boundary between the Pacific and North American plates. The driving stresses

behind plate motion persist across the lithosphere over geologic time [*Ghosh and Holt*, 2012]. The region boasts markedly rugged topography, as high as 3000 meters in the peaks of the San Bernardino Mountains, although considering the proximity to the strike-slip SAF, likely imparts only a minimal effect on stress modulation. Displacement rates from GPS and paleoseismic studies [e.g. *Bennett et al.*, 1996; *Dorsey*, 2002; *Frizzle et al.*, 1986; *Harden and Matti*, 1989; *Matti and Morton*, 1993; *Powell and Weldon*, 1992; *T Rockwell et al.*, 1990; *Sharp*, 1967; 1981; *Van Der Woerd et al.*, 2006; *R J Weldon and Sieh*, 1985] indicate that ~70% of total relative plate motion in southern California is accommodated by the SAF and San Jacinto fault (SJF) [*Bennett et al.*, 2004]; however, the region has not experienced a major earthquake in the last 300 years [*Grant and Lettis*, 2002; *R Weldon et al.*, 2005], and contemporary estimates suggest that stress accumulation along locked portions of the crust is approaching threshold levels [e.g. *Smith-Konter and Sandwell*, 2009]. While the rate of stress accumulation on major faults is well constrained by surface geodesy [e.g. *Burkhard et al.*, 2018; *Lisowski et al.*, 1991; *Smith and Sandwell*, 2003; *Smith-Konter and Sandwell*, 2009; *Tong et al.*, 2013], initial investigations suggest that loading rate heterogeneity by itself is not sufficient to fully explain the character of stress in the Cajon Pass region. Further integrative modeling of stress from multiple tectonic processes may be necessary to completely describe stress in this region.

Cajon Pass lies within the San Bernardino restraining bend in the SAF and marks the emergence of the SJF network (Figure 1). *Swanson* [2005] propose that fault adhesion or lock up of the linear Mission Creek SAF segment, driven by an increase in slip resistance associated with a change in local stress orientations on the preexisting structure, led to the formation of the curved San Bernardino SAF segment at the SBB. Development of this bend in the SAF system caused readjustment of regional strain partitioning forcing strain to be localized to the region surrounding the main SAF [*Li and Liu*, 2007]. Geologic and stratigraphic data [e.g. *Albright*, 1999; *Dorsey*, 2002] propose that the inception of the subparallel SJF accompanied the formation of the SBB in the SAF ca. 1.5 Ma, suggesting that the SJF may act as a bypass structure that reduces strain along the San Bernardino SAF segment [*Li and Liu*, 2007; *Matti and Morton*, 1993]. This shift is preserved in the difference in seismicity between each fault network; the SJF has ruptured in several earthquakes in the last century, whereas the southernmost SAF has been relatively quiescent [*T K Rockwell et al.*, 2015; *R Weldon et al.*, 2004]. Displacement rates [e.g. *Becker et al.*, 2005; *Bennett et al.*, 2004; *Meade and Hager*, 2005; *T Rockwell et al.*, 1990; *Van Der Woerd et al.*, 2006] show strong evidence for a tradeoff or codependence between each fault network. Increased slip on the SJF will lead to the eventual abandonment of the San Bernardino and Mission Creek segments of the southern SAF system and weaken its impact on regional crustal deformation [*Li and Liu*, 2007]. Compared to the SAF north of Cajon Pass faulting in this zone is diffuse, and the region may serve as the initiation of multistranded behavior observed on the SAF system south through the Salton Trough. Several major fault zones, including the San Andreas, San Jacinto, Elsinore Laguna Salada, and Eastern Transverse Ranges merge in this region (Figure 1a). The zone is persistently active (14 events in the last 1600 years) [*T K Rockwell et al.*, 2015] and characterized by a range of focal mechanisms [*Yang et al.*, 2012]. Paleoseismic studies provide evidence for a variety of rupture patterns that have both stopped and passed through the junction, involving slip on multiple fault segments other than the SAF [*Grant-Ludwig et al.*, 2015; *Onderdonk et al.*, 2015; *T K Rockwell et al.*, 2015], and suggest that the area may serve as a behavioral boundary on multifault ruptures. Dynamic rupture simulations confirm single event, multifault ruptures at Cajon Pass, but are most strongly influenced by background stress heterogeneity, with greater heterogeneity producing shorter ruptures [*Lozos*, 2016; *Lozos et al.*, 2015]. The possibility for

large multifault ruptures at Cajon Pass represents a high potential seismic hazard and earthquake risk for southern California. Any resolved understanding of the characteristics of stress at Cajon Pass may inform future rupture scenarios.

Estimates for the orientation of the *in situ* stress field across southern California are well constrained by recent seismicity [*Yang and Hauksson*, 2013], and while they generally indicate a right lateral strike-slip faulting regime across Cajon Pass, there are several anomalous regions where the orientation deviates from this behavior. The sources of these anomalous regions remain unresolved. While active faulting contributes to local heterogeneities in stress, it is not the only process [*Yang and Hauksson*, 2013]. Other active processes such as differential fault loading, gravitational sinking and collapse, and heterogeneity in the plate driving stress influence the regional and local style of heterogeneities (Figure 2a).

Direct measurements of crustal stresses near Cajon Pass are available from borehole breakouts [*Shamir and Zoback*, 1992; *Zoback and Healy*, 1992], but lack density of coverage. These estimates are limited to the upper 3.5 km of the crust and it remains unresolved how this stress reflects or affects stress at depth, thus earthquake scientists heavily rely on models to estimate stress at seismogenic depths [*Zoback et al.*, 2010]. With the goal of fully characterizing the state of crustal stress, there exist mature component models for stress from various geodynamic processes at Cajon Pass, including locked fault stress accumulation rates [e.g. *Burkhard et al.,* 2018] and topographic load stress [e.g. *Luttrell and Smith-Konter,* 2017].

In this study, we propose to incorporate existing models of stress from individual geodynamic processes [i.e. *Burkhard et al.,* 2018; *Luttrell and Smith-Konter,* 2017] to develop a forward model of stress state at Cajon Pass to investigate the sources of stress field heterogeneity (Figure 2). We consider any combination of plate driving stress, stress accumulation on locked faults, and stress from topography capable of reproducing the anomalous stress orientation features observed in the modern field indicated by focal mechanisms [*Yang and Hauksson*, 2013] (Figure 3) to evaluate the relative importance of each process in determining the overall stress state at Cajon Pass.

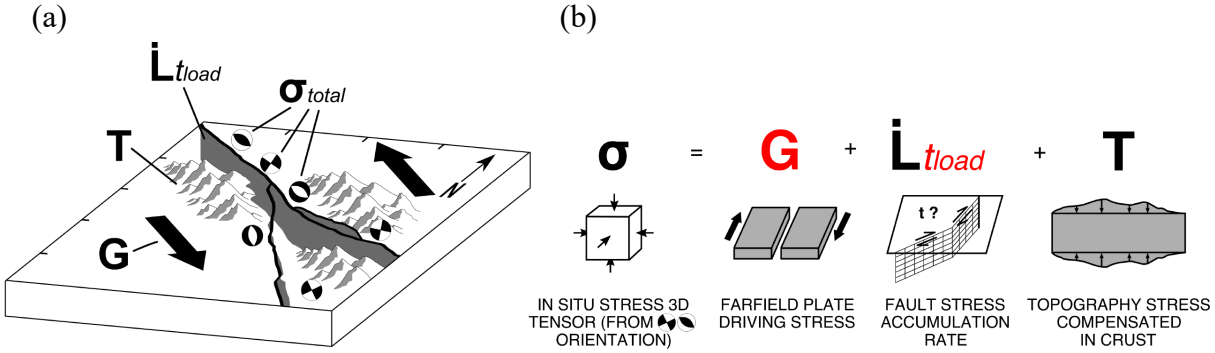

Figure 2. Components of stress considered in this study. (a) Cartoon representation of stressing processes at Cajon Pass. (b) Mathematical schematic of forward model. *In situ* stress (σ) is a combination of geodynamic plate driving stress (G), the stress accumulation rate on locked fault segments (L̇) acting over some loading time (t_{load}), and stress from built topography (T). Red denotes free parameters.

We hypothesize that the driving stress may rotate along major fault segments in the Cajon Pass region. To address this, we determine the driving stress orientation on each fault segment capable of most closely approximating the orientation of the modern field inferred by focal mechanisms, to determine if a single uniform tectonic stress field can best fit the region entirely.

2. Methods

2.1. Stress Orientations to be Reproduced

By assuming that seismicity across California occurs in response to plate boundary stresses localized on fault structures, *Yang and Hauksson* [2013] use the inversion of recent focal mechanisms to estimate the three-dimensional deviatoric stress tensor across southern California (see Appendix A). *Yang and Hauksson* [2013] use maps of maximum horizontal compressive stress orientation (SHmax) and the style of faulting (Aphi) to identify significant regional and local heterogeneities in stress across southern California. In this study we consider the resulting stress field in the Cajon Pass region to represent the *in situ* state of stress in the crust. Cajon Pass consists of many local stress heterogeneities that vary in spatial scale from 10-60 km, and degree of heterogeneity, and frequently change along the surface traces of major faults (Figure 3).

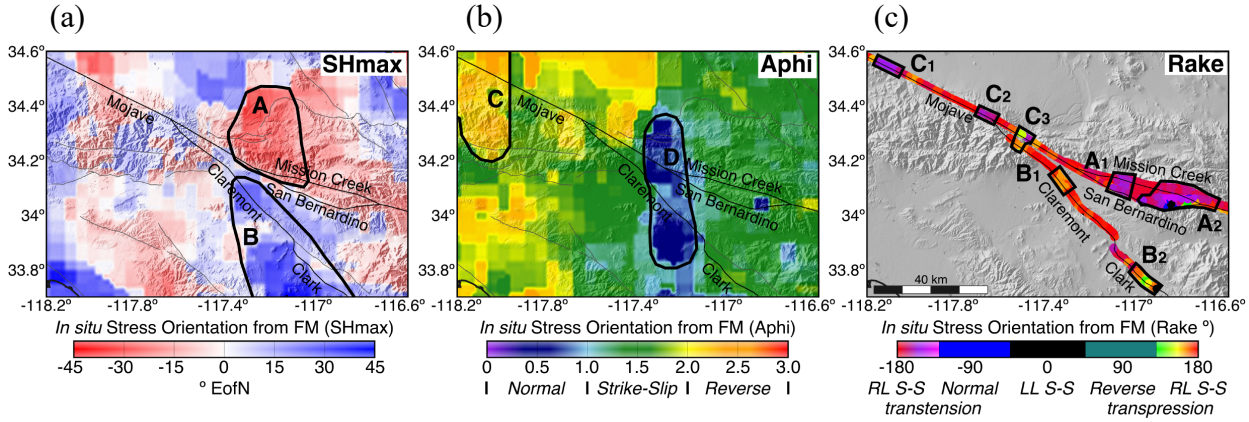

Figure 3. Stress orientation from focal mechanisms [*Yang and Hauksson,* 2013]. (a) SHmax azimuth of stress field derived from earthquake focal mechanisms. (b) Aphi of stress field derived from earthquake focal mechanisms. (c) Predicted rake angle of stress field derived from earthquake focal mechanisms resolved on to fault surfaces shown in Figure 1b. Black polygons represent features we aim to recreate with our forward model and are named according to their corresponding features present in (a) and (b).

Stress heterogeneities in SHmax include two large wedge-shaped regions that are well confined by neighboring fault traces (A and B in Figure 3a). In contrast to relatively north-south background orientations, SHmax directions rotate ~30º counterclockwise and clockwise at wedge A and B respectively. Stress heterogeneities in Aphi include a patch of reverse faulting on the northern Mojave segment (C in Figure 3b), and a patch of normal faulting stress regime in the San Bernardino Mountains (D in Figure 3b). Neither faulting anomaly is bounded by fault traces; however, anomaly D is located in the area where the SJF emerges and branches from the SAF southeastward.

Many of these local heterogeneities cross major SAF and SJF segments and it is useful to interpret how they might manifest on the faults themselves. We predict the rake angles (outlined in Appendix B) for the *Yang and Hauksson* [2013] stress estimate on major Cajon Pass fault

surfaces in Figure 3c. On major Cajon Pass fault segments, we observe rake angles according to primarily right lateral strike-slip behavior, as expected for the SAF (Figure 3c). We recognize several local stress heterogeneities in predicted rake angle (black polygons in Figure 3c) that are well aligned with features observed in SHmax and Aphi maps (black polygons in Figures 3a and 3b). These features vary in fault length (from 5 to 25 km), orientation, and degree of deviation from overwhelmingly right lateral values predicted for the region (Figure 3c). We observe four transtensional regions on SAF segments (C_1, C_2, A_1, and A_2 in Figure 3c), that vary from the surrounding strike-slip values an average of 21º, 12º, 17º, and 37º, respectively, towards normal behavior. We also recognize three transpressional regions beginning at the onset and continuing along the SJF (C_3, B_1, and B_2 in Figure 3c) that vary an average of 36º, 12º, and 44º, respectively, towards reverse behavior. Complete information regarding rake angles predicted in these regions is provided in Table 1.

Table 1. Rake angles predicted for stress field inferred from focal mechanisms.

Feature	Average Predicted Rake Angle (º)	Absolute Difference from RL S-S Behavior (º)
C_1	-159	21
C_2	-168	12
C_3	+144	36
A_1	-163	17
A_2	-143	37
B_1	+168	12
B_2	+136	44

The sources of these anomalous regions remain unresolved. There are several important aspects, including complex subsurface 3D fault structure, a major rotation in SAF strike, and the emergence of the SJF that may contribute to the observed patterns in rake at Cajon Pass. If stress heterogeneity were principally controlled by local fault motion then we expect the location, degree, and spatial scales of stress field variability to reflect this [*Yang and Hauksson*, 2013]. *Yang and Hauksson* [2013] suggest that movement on adjacent right lateral strike-slip faults may drive local heterogeneities in stress; however, this framework does not explain the clockwise SHmax rotation in B (Figure 3a) or the Aphi anomalies (Figure 3b).

2.2. Processes Contributing to the *in situ* Stress Field

The modern three-dimensional *in situ* crustal stress field is the sum of accumulated stress from multiple tectonic processes acting over a myriad of spatial and temporal scales (Figure 2a). We assume that the total stress field at Cajon Pass, σ, can be divided into three independent components (Figure 2b) (An extended summary of each of these components is presented in Appendix A; a brief summary follows below). G represents the tectonic driving stress field applied to the lithosphere over geologic time as well as any other stress contributions within the crust not explicitly considered. $\dot{L}t_{load}$ represents the accumulation of stress along locked fault segments throughout the earthquake cycle ($\dot{L}$ denotes the rate of stress accumulation [*Burkhard et al.*, 2018]

and t_{load} corresponds to the associated loading times [*T K Rockwell et al.*, 2015; *R Weldon et al.*, 2004]). T represents stress contributed by modern topography built up as a result of inelastic deformation over millions of years [*Luttrell and Smith-Konter*, 2017]. Stress estimates from focal mechanisms [*Yang and Hauksson*, 2013] are calculated from a 30-year seismicity catalog. If we assume that topography is not actively changing over this timescale, as in *Luttrell and Smith-Konter* [2017], the main forces in our model do not change. Additionally, we consider that each process operates over such different timescales that there is no feedback between processes, and we can consider each as an independent process. Consequently, we are able to model the modern *in situ* crustal stress field by the addition of stress components from each individual process. In our approach stress components from G and $\dot{L}t_{load}$ are two-dimensional. Therefore, any vertical components of stress in σ must be generated by the contribution of topography.

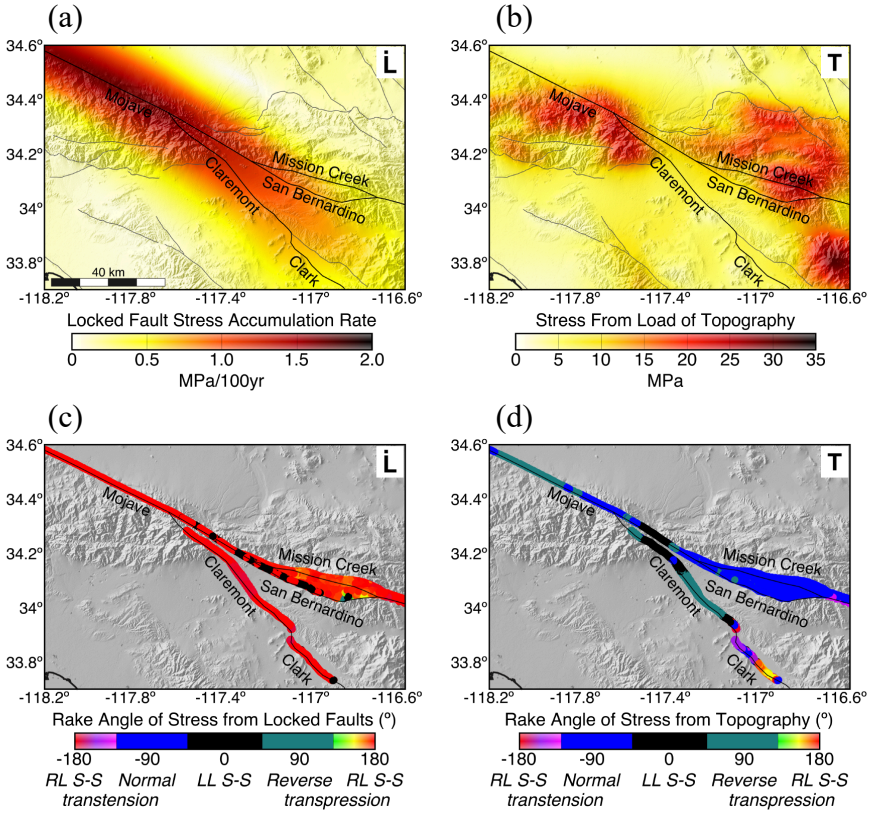

Figure 4. Stress estimates from existing models for locked faults [*Burkhard et al.*, 2018] and topography [*Luttrell and Smith-Konter,* 2017] at seismogenic depth. (a) Stress accumulation rate due to loading of locked fault segments. (b) Magnitude of stress from topography. (c) Predicted rake angle on fault surfaces due to stress accumulation on locked faults. (d) Predicted rake angle on fault surfaces due to stress field from load of topography.

Figures 4a and 4b show estimates of stress accumulation rate due to loading of locked fault segments [*Burkhard et al.*, 2018] and estimates of stress magnitude from topography [*Luttrell and Smith-Konter*, 2017] (See Figure A1 for orientations of stress of these components). Figures 4c

and 4d show the predicted rake angle along fault surfaces due to each of these components. It is clear that neither component can independently reproduce rake anomalies shown in Figure 3c.

2.3. Forward Model for Crustal Stress

We combine the individual components described above into a modeled composite stress field with three free parameters. We allow driving stress magnitude (G_{dS}), and orientation (G_{θ}), as well as effective loading times (t_{load}) on locked faults to vary along five fault segments (Figure 1b): the Mojave, San Bernardino, Mission Creek, Claremont, and Clark segments. We consider driving stress orientations from -45 to 45º EofN, driving stress magnitudes from 0 to 30 MPa, and effective loading times of each fault segment from 0 to 3000 years. Ideally, t_{load} should resemble the time since last rupture if the most recent earthquake achieved complete stress release.

We treat composite stress fields as a forward model. Stress estimates are resolved onto main SAF/SJF fault surfaces from the Southern California Earthquake Center Community Fault Model v. 5.2 [*Nicholson et al.*, 2017] to predict the associated rake angles (outlined in Appendix B). Rake in this study is regarded as the angle between fault strike and maximum shear stress direction within the fault plane, measured counterclockwise from strike direction, from -180 to 180º [*Aki and Richards*, 2002]. We compare predicted rake angle orientations of each model run with that indicated by focal mechanisms [*Yang and Hauksson*, 2013], and effective loading times on each fault segment with paleoseismic estimates [*T K Rockwell et al.*, 2015; *R Weldon et al.*, 2004] (Table 2).

Spatial volumes for comparison include triangulated surfaces for five distinct fault segments (Mojave, San Bernardino, Mission Creek, Claremont, and Clark in Figure 1b) from the Southern California Earthquake Center Community Fault Model v. 5.2 [*Nicholson et al.*, 2017], named according to *Burkhard et al.* [2018]. The Community Fault Model provides a three-dimensional representation of active faults in southern California based on seismicity, seismic reflection profiles, wells, and geologic cross sections [*Nicholson et al.*, 2017]. Complete information regarding fault surfaces from the Community Fault Model is provided in Appendix A. Each component of stress we consider is depth independent and calculated at median seismogenic depth. Consequently, by sampling two-dimensional stress along three-dimensional fault planes, we only incorporate two-dimensional variations in fault locations. We collapse the seismogenic zone into a fully 2D region, at median depth (~5-10 km), principally driven by the three-dimensional fault geometries expressed at this surface. Three-dimensional fault surfaces at depth are projected to a single surface representing the middle of the seismogenic zone. Most fault segments are nearly vertical; however, the Mission Creek and San Bernardino segments dip enough (to the northeast) to be seen in map view projections (i.e. wider fault segments in Figure 3c).

Models are evaluated by the ability to reproduce the anomalous rake features observed in the focal mechanism estimate (C_1, C_2, C_3, A_1, A_2, B_1, B_2 in Figure 3c). We consider the mean absolute difference between focal mechanism predicted rake angles and our composite model estimates on each fault segment to designate a single quantity for the degree of fit. Low mean rake angle difference values correspond to better fitting models. Models were previously evaluated with the scalar misfit parameter, E, defined by *Luttrell and Smith-Konter* [2017]; however, we ultimately found that rake angle was a better metric to classify model fit (see Appendix C for previous results).

We determine the best fitting model with discrete values for G_{θ}, G_{dS}, and t_{load} on each fault segment independently. If all fault segments can be best fit with similar driving stress orientations (i.e. $G_{\theta\ \mathrm{MOJAVE}} = G_{\theta\ \mathrm{SAN\ BERNARDINO}} = \ldots$) and loading times consistent with paleoseismic estimates

for last rupture, then the patterns of heterogeneity in $\dot{L}$ and T may be sufficient to explain the heterogeneity observed in the modern field. If not, then an additional source of stress heterogeneity is required and may regulate future rupture behavior. In this approach the maximum level of spatial stress heterogeneity we consider is on the scale of fault segments (from 30-100 km in this region).

3. Results

In Figure 5 we explore model fit across our parameter space for the San Bernardino fault segment. Figure 5a shows 2º contours of mean predicted rake angle difference between stress estimates from focal mechanisms and forward models with a driving stress magnitude of 10 MPa and variable driving stress orientations (G_θ) and loading times (t_{load}) on locked fault segments. We find that along the San Bernardino segment best fitting models correspond to a discrete range of driving stress orientations (~20º EofN) (Figure 5a). As driving stress orientations trend away from this region model fit decreases significantly (Figure 5a). The San Bernardino segment displays considerable sensitivity to effective loading time and the fit improves with longer loading (Figure 5a). Best fitting models exist at loading times (>1900 years) much longer than that if it has only been accumulating stress since the timing of last rupture (star in 5a).

Figure 5b shows minimum mean rake angle difference as a function of load times on the San Bernardino segment for different driving stress magnitudes. We observe that overall fit to focal mechanism rake orientations improve with increased driving stress magnitude, up to 30 MPa, the highest input we consider (Figure 5b).

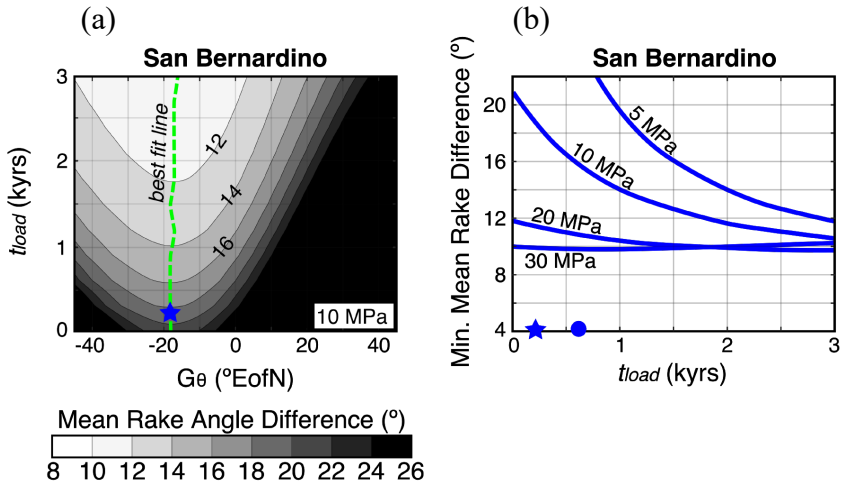

Figure 5. Model fit across parameter space for San Bernardino fault segment. (a) 2º contours of mean predicted rake angle difference between stress estimates from focal mechanisms and forward models with a driving stress magnitude G_{dS} =10 MPa and variable driving stress orientations (G_θ) and loading times (t_{load}) on locked fault segments. Best fit line (green dashed) indicates driving stress orientations that minimize misfit at each locked fault loading time. (b) Minimum mean rake angle difference as a function of load times on the San Bernardino segment, using different driving stress magnitudes as indicated. Stars indicate the time since last rupture on the San Bernardino fault segment [*R Weldon et al.*, 2004], and circle represents the loading time that produces the absolute best fit for the San Bernardino segment.

Complete contours, as in Figure 5a, for all five segments for multiple driving stress magnitudes can be viewed in Figure D1. We find that the best fitting driving stresses exist at variable widths and locations (ºEofN) along individual fault segments (Figure D1). Claremont and Clark segments

are best fit with a narrow range (~20º) of north-northeast driving stress orientations (Figure D1). The Mission Creek and San Bernardino segments can be best fit with a wider range (~40º) of north-northwest trending driving stresses (Figure D1). The Mojave segment is best fit for the widest range of G_θ (~60º), oriented north-northwest, but only at large loading times (Figure D1). Along each fault segment we observe that the range of best fitting G_θ shrinks with loading times approaching the timing of last rupture (stars in Figure D1). We find that along each individual fault segment, the best fitting models exhibit a tradeoff between driving stress magnitude and orientation. As we increase driving stress magnitude overall model fits improve; however, the range of driving stress orientations capable of minimizing misfit decreases (Figure D1).

We explore the effect of driving stress magnitude on model fit for all fault segments in Figure D2. We observe that individual fault segments are variably sensitive to driving stress magnitude (Figure D2). The Mission Creek is most sensitive, with sensitivity decreasing along the San Bernardino, Mojave, Claremont, and Clark segments (Figure D2). As in Figure 5b, we find that overall fit to focal mechanism rake orientations improve with increased driving stress magnitude on the Mojave, San Bernardino, Mission Creek, and Claremont segments (Figure D2). Our models with the poorest fit occur along the Clark segment, where model fit displays essentially no sensitivity to driving stress magnitude (Figure D2).

Figure 6 shows maps of absolute rake angle difference from the best fitting model on each segment with a uniform geodynamic stress and loading times taken from paleoseismic estimates (stars in Figure D1 and D2). Complete information regarding these models is provided in Table 2.

Table 2. Best fit paleoseismic loading models. Models capable of minimizing misfit to focal mechanism estimates at each fault segment with loading times drawn from paleoseismic estimates of last rupture. If complete coseismic stress release, then fault segments have only been accumulating stress since the time of last rupture. 'Ages of Last Rupture' are applied to *Burkhard et al.* [2018] stress accumulation rate estimates to define the paleoseismic loading profile used in Figure 6.

Best Fitting Model for each Fault Segment with Paleoseismic Load Time

Fault Segment	Age of Last Rupture (yrs)	Reference	G_θ (ºEofN)	G_{dS} (MPa)	Misfit Average Predicted Rake Angle Difference (º)
Mojave	162	*Weldon et al.*, 2004	-17	30	12.2
San Bernardino	207	*Weldon et al.*, 2004	-7	30	10.0
Mission Creek	293	*Weldon et al.*, 2004	-18	30	7.5
Claremont	120	*Rockwell et al.*, 2015	10	30	5.4
Clark	101	*Rockwell et al.*, 2015	10	30	16.1

We observe that rake angles predicted from these models are consistently suggestive of right lateral strike-slip behavior (rake angle ~ ±180º) along the entirety of fault surfaces. As such, we observe the largest absolute rake angle difference values in regions corresponding to locations of the largest deviations from right lateral strike-slip behavior observed in the focal mechanism estimate (black polygons in Figure 6). We find that the ability of these models to recreate the patterns of stress observed in the modern field varies along each fault segment (Figure 6 and Table

2) but is principally controlled by the existing degree of deviation from right lateral behavior in the focal mechanism estimate (i.e. we can most closely approximate right lateral and near right lateral features).

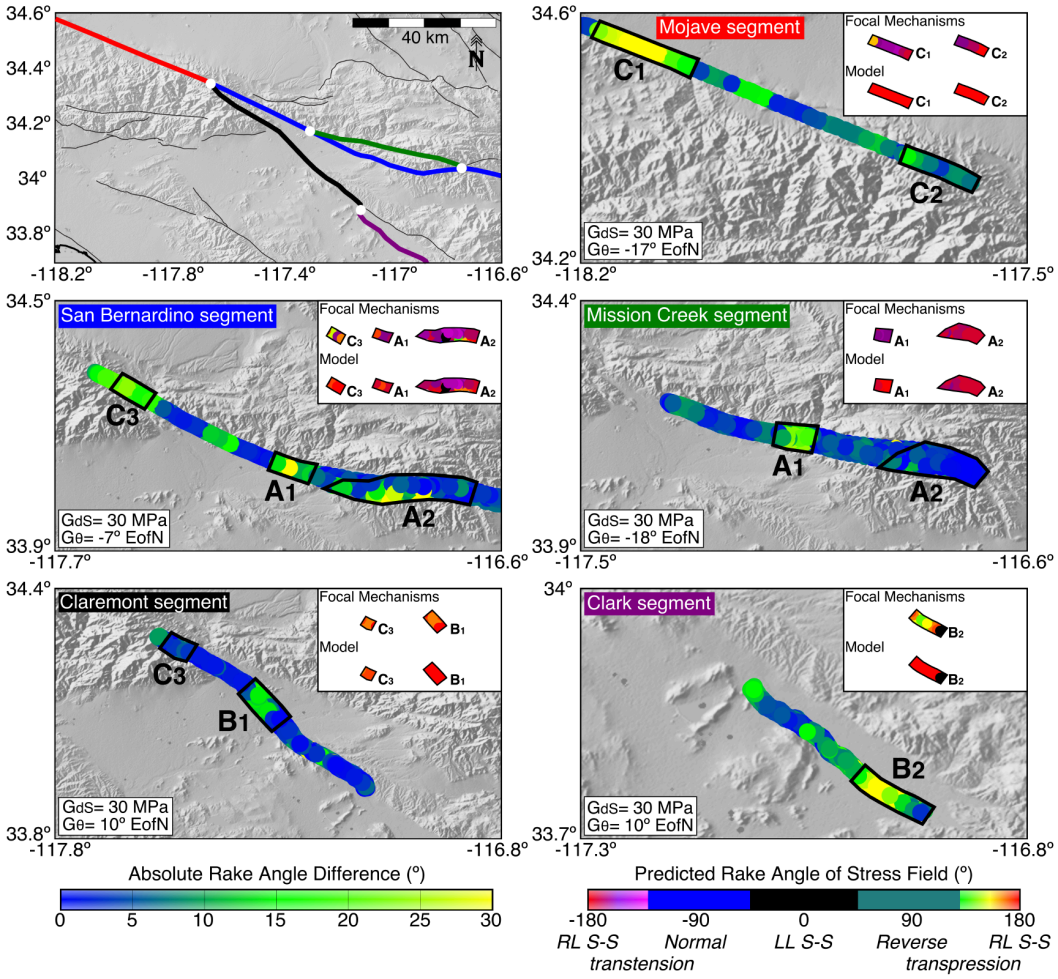

Figure 6. Misfit for paleoseismic loading models. Maps of absolute rake angle difference from the best fitting model on each segment with a single uniform geodynamic driving stress and locked fault loading times taken from paleoseismic estimates (Table 2). Black polygons denote the location of rake features present in the focal mechanism estimate that we attempt to resolve. Inset in each map shows the predicted rake angles from focal mechanisms and each model in the locations of features we aim to recreate.

If the patterns of stress heterogeneity in the modern field inferred from focal mechanisms are due to T and $\dot{L}$, then G should resemble a uniform field of a single G_θ. We examine the best fitting model parameters for all fault segments together in Figure 7 to determine if a single driving stress can optimize fit along all fault segments. Figure 7a shows lines of best fitting G_θ and t_{load} on all fault segments (best fit lines in Figure D1). As mentioned previously, best fitting G_θ exist at variable locations for each fault segment (Figure 7a and D1). Best fitting driving stresses trend

principally north-northwest for SAF Mojave (-16º EofN), San Bernardino (-7º EofN), and Mission Creek (-16º EofN) segments, and north-northeast for SJF Claremont (10º EofN) and Clark (13º EofN) segments (Figure 7a). We notice a slight positive relationship between G_θ and t_{load} (i.e. as driving stress trends further east longer loading times are required to best fit the focal mechanism estimate); however, no single driving stress orientation can minimize misfit on all fault segments together (Figure 7a). Lines of best fit (i.e. Figure 7a) at all driving stress magnitudes considered are available in Figure D3.

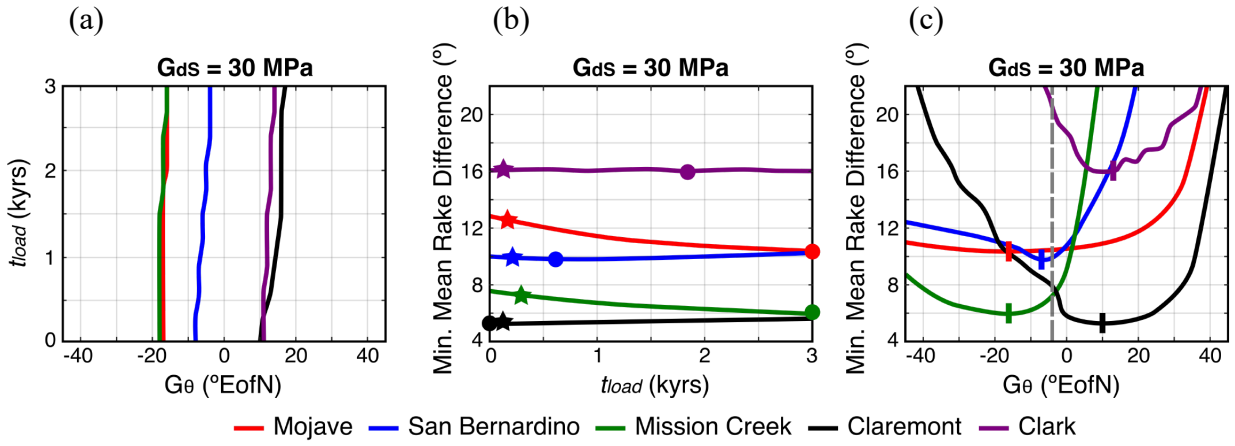

Figure 7. Best fitting model parameters for all fault segments. (a) Lines of best fitting G_θ and t_{load} on all fault segments (b) Minimum mean rake angle difference for best fitting load times for all five segments. Stars indicate the time since last rupture (Table 2) and circles indicate the loading time required in our best fitting models for each segment (Table 3a). (c) Lines of minimum mean rake angle difference for best fitting driving stress orientations for all five segments. Gray dashed line indicates the driving stress orientation (G_θ=-4º EofN) required for a forward model to best match focal mechanism rake angle estimates on all five segments together with a single uniform driving stress. Vertical bars indicate the G_θ for the best fitting model on each individual fault segment.

Figure 7b shows lines of minimum mean rake angle difference as a function of best fitting load times on all fault segments. Contrary to the relationship between driving stress orientation and model fit in Figure 5a, no distinct region of loading times produces best fitting models. We observe that model fit is optimized at some threshold loading time, after which fit marginally improves (Figure 7b). The Mojave and Mission Creek segments are best fit with loading ~3000 years (circles in Figure 7b), much longer (~2800 years) than if stress has only been accumulating on these faults since the time last rupture (stars in Figure 7b). Best fitting load times (circles in Figure 7b) on the Claremont (0 years) and San Bernardino (600 years), most closely approximate paleoseismic estimates for last rupture (stars in 7b). The Clark segment can be best fit with intermediate loading (purple circle in Figure 7b), ~1800 years, much longer than the estimate for last rupture (purple star in 7b); however, it is worth mentioning that Clark models consistently predict high misfit to focal mechanism rake estimates and display essentially no sensitivity to changes in t_{load}.

We note that our best fitting models prefer large driving stress components (30 MPa) that ultimately dampen the contribution from increased time of stress accumulation on locked faults. Consequently, in Figure 7b we observe a minimal effect of t_{load} on model fit. To explore the effect of fault segment loading time on model fit we consider models incorporating lower driving stresses (where t_{load} exerts a greater impact on the composite stress model than in Figure 7b models) in Figure D4. Figure D4 shows lines of mean rake angle difference as a function of load times on all fault segments for all driving stress magnitudes. We observe, that for models incorporating low driving stresses, <10 MPa, overall model fits improve on the Mission Creek, Mojave, San Bernardino, and Claremont segments with increased t_{load} (Figure D4). At low driving stresses the Clark segment maintains low sensitivity, as observed in Figure 7b, to changes in effective load time (Figure D4). As mentioned previously, the response of model fit to increased load time diminishes as larger driving stress magnitudes are incorporated into composite stress fields (Figure D4).

Table 3. Best fitting models. (a) Best fitting model with segment-scale driving stress heterogeneity. Models capable of minimizing misfit to focal mechanism estimates at each fault segment. (b) Best fitting model with uniform driving stress. Model capable of minimizing misfit to focal mechanism estimates for all fault segments together with a single uniform driving stress (gray dashed line in Figure 7c). 'Loading Times' are applied to *Burkhard et al.* [2018] stress accumulation rate estimates to define the loading profiles used in Figure 8.

(a) Best Fitting Model with Segment-Scale Driving Stress Heterogeneity

Fault Segment	G_θ (ºEofN)	G_{dS} (MPa)	Loading Time (yrs)	Misfit Average Predicted Rake Angle Difference (º)
Mojave	-16	30	3000	10.2
San Bernardino	-7	30	600	9.8
Mission Creek	-16	30	3000	5.9
Claremont	10	30	0	5.2
Clark	13	30	1800	16.0

(b) Best Fitting Model with Uniform Driving Stress

Fault Segment	G_θ (ºEofN)	G_{dS} (MPa)	Loading Time (yrs)	Misfit Average Predicted Rake Angle Difference (º)
Mojave	-4	30	3000	10.5
San Bernardino			1900	9.9
Mission Creek			3000	7.2
Claremont			0	7.9
Clark			3000	20.9

Figure 7c shows lines minimum mean rake angle difference as a function of best fitting driving stress orientations on all fault segments. We find that along individual fault segments mean rake angle difference values can be minimized to variables levels and prefer unique driving

stress orientations (Figure 7c). The lowest mean rake angle difference is achieved on the Claremont segment (5.2º) and increases from Mission Creek (5.9º), San Bernardino (9.8º), Mojave (10.2º), and Clark (16.0º) segments (Figure 7c). As suggested by Figure 7a, no single G_0 can minimize misfit on all fault segments jointly (Figure 7c). If a uniform driving stress exists across all Cajon Pass fault segments, we find that a stress field of 30 MPa with compression oriented -4º EofN (gray dashed line in Figure 7c) produces the lowest misfit along all fault segments (Figure 7c). This model, outlined in Table 3b, is referred to as our 'Best Fitting Model with Uniform Driving Stress.' We also consider a total model comprised of the best fitting model on each individual fault segment (circles in Figure 7b, vertical bars in Figure 7c), outlined in Table 3a, herein referred to as our "Best Fitting Model with Segment-Scale Driving Stress Heterogeneity."

4. Discussion

4.1. Implications for Stress Field Heterogeneity

In Figure 8 we evaluate the ability of our optimal models (Table 3) to create the patterns of stress heterogeneity observed in the focal mechanism rake estimate. Figure 8 shows maps of predicted rake angles for our best fitting model with a uniform driving stress (Figure 8a) and with segment-scale driving stress heterogeneity (Figure 8b), as well as maps of absolute rake angle difference between these fields and the focal mechanism estimate for the modern field (Figure 8b and 8c).

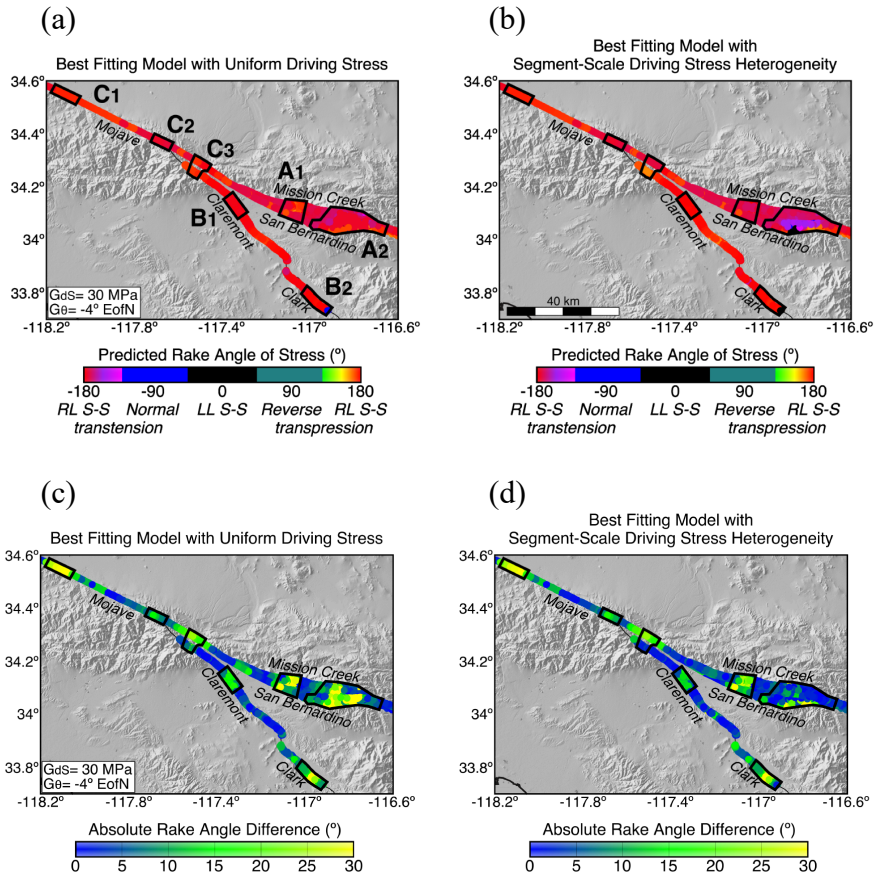

Figure 8. Results for best fitting models. (a,b) Maps of predicted rake angles of stress from best fitting model with a uniform driving stress (a) (Table 3b) and with segment-scale driving stress heterogeneity (b) (Table 3a). (c,d) Maps of absolute rake angle difference between focal mechanism estimate and stress from a and b. Black polygons represent locations of features present in the focal mechanism stress estimate that we attempt to resolve.

We find that stress estimates from our best fitting models maintain largely right lateral strike-slip rake values along the entirety of fault surfaces (Figure 8a and 8b). Consequently, these models consistently underproduce rotations in rake angle at the locations of major trantensional and

transpressional anomalies observed in the focal mechanism estimate (C_1, C_2, C_3, A_1, A_2, B_1, B_2 in Figure 3c). Both models predict largest misfit values at these features (black polygons in Figure 8c and 8d). Complete information regarding the magnitude of misfit for our optimal models at these features is provided in Table 4.

Table 4. Misfit for best fitting models. Average absolute rake angle difference in the regions of focal mechanism rake anomalies (black polygons in Figure 3c) between stress from focal mechanisms and stress from best fitting model with a uniform driving stress (Figure 8c, Table 3b) and best fitting model with segment-scale driving stress heterogeneity (Figure 8d, Table 3a).

Misfit at Rake Anomalies in FM Estimate for Best Fitting Models

Best Model	Average Absolute Rake Angle Difference (º)							
	C_1	C_2	C_3	A_1	A_2	B_1	B_2	Average
Uniform Driving Stress	27.7	11.1	15.6	23.7	16.7	16.6	36.1	21.1
Segment-Scale Driving Stress Heterogeneity	27.0	11.6	10.8	19.9	9.4	12.6	27.5	17.0
Improvement (+ %)	2.5	-4.5	30.8	16.0	43.7	24.1	23.8	19.5

We find that our best fitting model with segment-scale driving stress heterogeneity (Figure 8d) produces lower overall misfit values to the modern field than our best model with a uniform tectonic stress across the region (Figure 8c). We are able to decrease average absolute rake angle difference values at C_1 (2.5%), C_3 (30.8%), A_1 (16.0%), A_2 (43.7%), B_1 (24.1%), and B_2 (23.8%) with our model incorporating segment-scale heterogeneity in the driving stress (Table 4). At C_2, misfit increases for a model with driving stress heterogeneity by 4.5% (Table 4); however, average misfit along the entirety of the Mojave segment is minimized (Table 3). The effect of driving stress heterogeneity on model fit is most visible at A_2 (Figure 8c) where our best fitting model with a heterogeneous driving stress predicts an average absolute rake angle difference ~44% lower than with a homogenous driving stress (Table 4). Despite the ability to improve fit to the modern field, our model with segment-scale driving stress heterogeneity remains ineffective in recreating major rotations in rake angle observed in the focal mechanism estimate (black polygons in Figure 8d) (predicted absolute rake angle difference values are, on average, 17º in these regions).

We consider a wide range of combinations of two-dimensional components of stress. Any vertical components of stress must be generated by the contribution of topography, which we find to impart a minimal effect on overall composite fields (Figure 8a and 8b). It is possible that anomalous rake values in the modern field may be produced by other seismogenic processes (e.g. lithologic contrast, variable heat flow, or mantle flow anisotropy), external to those considered in

this study, that are expected to contribute significant vertical components of stress [*Hartog and Schwartz*, 2001; *Lachenbruch and Sass*, 1980; *Vernik and Zoback*, 1989]. Cores in the area indicate a significant change in lithology across the SAF to 3.5 km depth and a great diversity of rock types with varying degrees of alteration [*Silver and James*, 1988; *Vernik and Zoback*, 1989; 1992] that are expected to influence fault strength and stress accommodation [*Vernik and Zoback*, 1989]. Additionally, discrepancies in seismic velocities from the Southern California Earthquake Center Community Velocity Model suggest that this contrast may extend to 5 km depth [*Magistrale et al.*, 2000].

The observed patterns of modern stress heterogeneity may also be linked to spatial heterogeneity in orientation of the tectonic driving stress field at finer scales than we consider in this study (i.e. smaller than fault segment-scale, <~30-100 km). With our current approach our results suggest that heterogeneity at a scale of tens of kilometers, external to topography and locked faults, in the orientation of tectonic driving stress, another source not explicitly considered, or both, may be the dominant source of stress heterogeneity at Cajon Pass. If stress at Cajon Pass is strongly influenced by heterogeneity in the tectonic driving stress, and not fault local processes, we expect these effects to be long lived relative to the earthquake cycles on major SAF and SJF faults.

Evidence for heterogeneity in driving stress orientation across southern California is not unique. *Ghosh and Holt* [2012] present a global dynamic model for lithospheric stress within plates and at plate boundary zones, constrained by GPS, that includes the effects of topography, lithospheric structure, mantle flow, and lateral viscosity variations. This model has few pixels in southern California, but predicts that the tectonic driving stress orientation may rotate clockwise across the SAF [*Ghosh and Holt*, 2012]. Our best fitting models on each fault segment are consistent with a clockwise rotation in driving stress azimuth (from north-northwest to north-northeast) southward across the Cajon Pass area (Table 3a and Figure D5).

We also find that differential stress magnitudes for our best fitting model (measured as σ_1 - σ_3) are consistent with estimates from separate studies [e.g. *Luttrell and Smith-Konter*, 2017]. Stress magnitude is expected to vary with depth. As the inverted stress field from focal mechanisms is depth independent, so too are the fields calculated in this study. Our results are best interpreted as representing the middle of the seismogenic zone (~5-10 km depth). We predict average differential stress magnitudes of 93 MPa on the Mojave segment, 61 MPa on the San Bernardino segment, 62 MPa on the Mission Creek segment, 59 MPa on the Claremont segment, and 64 MPa on the Clark segment for our best fitting model. Our estimates are largely consistent with *Luttrell and Smith-Konter* [2017], who find that a differential stress at seismogenic depth in excess of 62 MPa is required at Cajon Pass. We predict the largest stress magnitudes on the Mojave segment, to be expected for long loading (3000 years in best fitting model) on the most rapidly accumulating segment (~2.0 MPa/100yr from *Burkhard et al.* [2018]) (Figure 4a).

Our best fitting models permit long load times on multiple faults segments, specifically 3000 years on the Mission Creek and Mojave segments, and 1800 years on the Clark (Table 3a). If fault segments achieve complete coseismic stress release, then stresses have only been accumulating since the timing of last rupture (Table 2). The allowance of large effective loading times an order of magnitude greater than paleoseismic estimates may suggest that Cajon Pass faults experience incomplete stress release during ruptures with residual stresses compounding over the earthquake cycle. We should mention that our models are more sensitive to changes in the representation of driving stress than effective loading times on faults. Mean rake angle differences from our best fitting models with loading times drawn from paleoseismic estimates (Table 2) are on average only ~10% higher than those from our best fitting model with unrestricted loading times (Table 3a).

Ultimately our results are constrained by representation of the modern stress field at Cajon Pass inferred from focal mechanisms by *Yang and Hauksson* [2013]. While recent seismicity may reflect stress at the time of rupture, it is possible this estimate does not represent the current state of stress in the crust as rupture events themselves may impose concurrent effects. Additionally, this estimate represents a smoothed field involving a regional-scale inversion of discrete earthquake events and may be limited by lack of seismicity or biased by few scattered events in some regions. For example, the normal faulting patch in the San Bernardino Mountains (D in Figure 3a) may have been generated by the Landers (1992) and Hector Mine (1999) earthquakes that triggered many aftershocks with normal faulting in the region between the two ruptures [*Yang and Hauksson*, 2013]. Furthermore, the *Yang and Hauksson* [2013] stress estimate is calculated from a 30-year catalog of seismicity. It is possible that anomalous features in this estimate may not be major or real over longer timescales (e.g. earthquake recurrence intervals, >100 years [*Fumal et al.*, 1993]).

At the Cajon Pass drillhole, direct measurements of stress from borehole breakouts predict SHmax oriented ~55º EofN [*Shamir and Zoback*, 1992; *Zoback and Healy*, 1992], in marked disagreement with ~-11º EofN predicted from focal mechanisms [*Yang and Hauksson*, 2013], and ~-7º EofN from our best fitting model with a uniform tectonic stress. It is worth noting that disparities in sampling depth, generally 0-20 km for focal mechanisms [*Yang and Hauksson*, 2013] and 0-3.5 km for borehole breakouts [*Shamir and Zoback*, 1992; *Zoback and Healy*, 1992], make defining a collective interpretation method difficult.

Yang and Hauksson [2013] provide uncertainties in SHmax orientation for their crustal stress estimate (Figure B1). In Cajon Pass, uncertainties in SHmax are frequently less than 1º but do reach a maximum of 5º in a 10 km^2 region northeast of the junction between the SAF and SJF (Figure B1a). We find that a ±5º change in SHmax for their focal mechanism stress estimate results in a 2.8º difference in mean predicted rake angle on Cajon Pass fault surfaces (Appendix B, Figure B1b).

4.2. Implications for Cajon Pass Earthquake Gate

The magnitude of shear stresses acting on the SAF is a subject of controversy. Heat flow measurements suggest that the level of shear stress on the seismogenic SAF is between 10-20 MPa [*Brune et al.*, 1969], and when considering the high angle between the axis of far-field compression and SAF strike, have been used to argue that the SAF represents a weak fault that operates at relatively low stresses [*Mount and Suppe*, 1987]. Evidence from laboratory derived coefficients of friction alternately predict that shear stresses on the SAF may be as much as five times larger than those predicted from heat flow data [*Zoback and Healy*, 1992]. This discrepancy is termed the San Andreas stress—heatflow paradox [*Hartog and Schwartz*, 2001; *Zoback and Healy*, 1992].

Our models are constructed at a single depth that we use to represent that seismogenic zone, and although we expect stress to vary with depth, it is useful to predict the maximum shear stresses of our best fitting models onto individual fault planes. The magnitude of stress in our models is solely controlled by representation of driving stress magnitude. Accordingly, predicted shear stress magnitudes will scale proportionally to this value, G_{dS}. We observe that model fit improves up to a threshold of ~30 MPa; however, without any indication of stress magnitude from the inversion of focal mechanisms to constrain this value, G_{dS} could be different. Therefore, for our models, it is most useful to look at the relative magnitudes and distribution of maximum shear stress on fault segments at Cajon Pass.

In Figure 9 we determine the maximum shear stress on major fault surfaces for our "Best Fitting Model with Uniform Driving Stress" (Figure 9a) and our "Best Fitting Model with Segment-Scale Driving Stress Heterogeneity" (Figure 9b). Maximum shear stresses predicted from our best fitting models suggest a non-uniform stress distribution (Figure 9). Shear stresses for our best fitting model with a uniform driving stress are in excess of ~40 MPa on the Mojave, Claremont, Clark, and northern San Bernardino segments; however, respectively low, ~15 MPa, on the Mission Creek and southern San Bernardino (Figure 9a). These results are consistent with the idea that the SJF network may have formed to accommodate plate boundary stresses non-optimally aligned with preexisting SAF segments immediately south of the San Bernardino restraining bend [*Matti and Morton*, 1993]. When we incorporate segment-scale driving stress heterogeneity, our best fitting model predicts a contrasting distribution and level of maximum shear stresses on major SAF/SJF fault segments (Figure 9b). We observe an increase in shear stress on the Mojave and Mission Creek segments, as well as a decrease on the northern sections of the San Bernardino and Claremont segments (Figure 9b). The most striking feature is the juxtaposition of high and low shear stresses, at the emergence of the SJF, between the southern Mojave (~60 MPa), and northern San Bernardino (~30 MPa) and Claremont (~10-20 MPa) segments (Figure 9b).

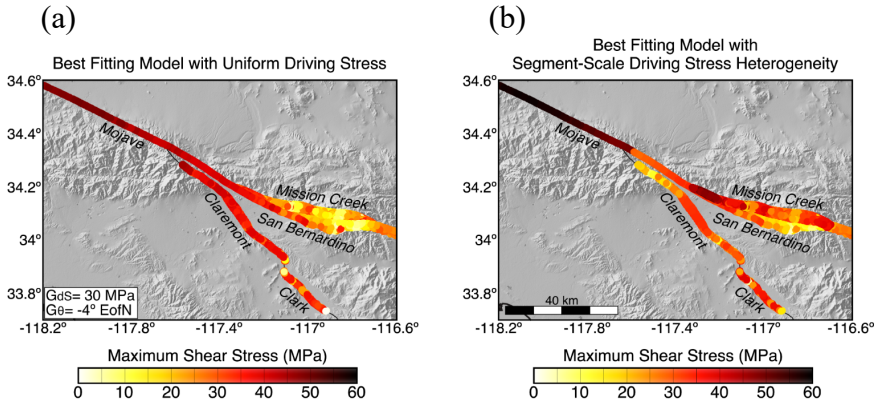

Figure 9. Shear stresses for best fitting models. (a,b) Maps of maximum shear stress predicted on fault surfaces for stress from best fitting model with a uniform driving stress (a) (Table 3b) and with segment-scale driving stress heterogeneity (b) (Table 3a).

Without clearer resolution for respective fault strengths or the depth-dependence of our models it is increasingly difficult to determine the current state of the Cajon Pass earthquake gate. If we assume uniform fault strength for all segments, likely not the case given complex fault geometries and variable rock types, the observed variations in resolved shear stress on Cajon Pass fault surfaces indicate that heterogeneity in tectonic driving stress orientation may inhibit multifault ruptures across the region.

5. Conclusions

We analyze stress at Cajon Pass with a forward model that considers combinations of tectonic driving stress, stress accumulation on major locked fault segments, and stress from built topography. This model is used to investigate the role of these processes in producing the lateral heterogeneity observed in the predicted rake angles for the *in situ* stress field indicated by earthquake focal mechanisms, as well as identify any potential heterogeneity in the regional tectonic driving stress field. We determine the driving stress orientation, magnitude, and effective loading time on five fault segments required to best fit the focal mechanism estimate.

Despite incorporating unique tectonic stress fields and loading profiles, stress estimates from our models maintain largely right lateral rake values along the entirety of fault surfaces. Even when considering stress combinations that most closely approximate the modern field in our optimal models, right lateral strike-slip behavior is sustained, and consequently we fall short in recreating the transtensional and transpressional rake anomalies observed in the focal mechanism estimate.

Models incorporating fault segment-scale heterogeneity in the orientation of tectonic stress produce lower overall misfit values than for models with a uniform tectonic stress orientation across the region. Despite this, rake angles predicted from these models consistently underproduce major rotations in rake observed in the modern field (i.e. largest misfit values remain concentrated in the regions of major focal mechanism rake anomalies). With our current approach, this may suggest that these features are generated by finer than fault segment-scale driving stress orientation heterogeneity (tens of kilometers).

Considering the best fitting models on each fault segment individually, we find that segments prefer unique driving stress orientations, particularly north-northwest on SAF segments and north-northeast on SJF segments, consistent with a clockwise rotation in stress orientation southward across the Cajon Pass region. Stress from our best fitting models estimate *in situ* differential stress magnitudes between 59 and 93 MPa in this area. Additionally, individual fault segments prefer tectonic differential stress magnitudes of at least 30 MPa and permit loading times in excess of 1700 years longer than paleoseismic estimates for last rupture on some segments to most closely approximate the modern stress field. The latter of which may suggest that fault segments in this region experience incomplete coseismic stress release during major rupture events.

Our results indicate that heterogeneity on the scale of tens of kilometers in the orientation of tectonic driving stress, another source not explicitly considered, or both, may be the dominant source of stress heterogeneity at Cajon Pass. We expect these effects to be long lived relative to the earthquake cycle on major SAF and SJF faults. We find that variations in resolved shear stress on Cajon Pass fault surfaces indicate that heterogeneity in tectonic driving stress orientation may inhibit multifault ruptures across the region. Further clarification of the sources of spatio-temporal driving stress heterogeneity and the resulting sensitivity of active fault segments in the region is necessary to improve seismic hazard and risk in this complex zone.

Appendix A. Model Inputs

Our forward model incorporates estimates for stress at Cajon Pass from existing models of individual tectonic processes. Full information regarding the methods and constraints utilized in each model can be referenced in the respective literature (e.g. *Yang and Hauksson* [2013]; *Luttrell and Smith-Konter* [2017]; *Burkhard et al.* [2018]). Below we provide summaries of each model for the purpose of contextualizing our approach.

(σ) *In Situ* Stress Field: *Yang and Hauksson* [2013]

In this work we utilize the *Yang and Hauksson* [2013] model to represent the current state of crustal stress at Cajon Pass. *Yang and Hauksson* [2013] use 179,000 high quality focal mechanisms from *Yang et al.* [2012] 1981-2010 California seismicity catalog, to invert, by methods of *Hardebeck and Michael* [2006], for the normalized deviatoric stress tensor. The resulting smoothed field spans southern California with 5-10 km spatial resolution. The model provides an estimate for the three-dimensional stress ellipsoid shape and orientation at seismogenic depth but provides no magnitude information.

(T) Stress from Topography: *Luttrell and Smith-Konter* [2017]

In this study we adopt the *Luttrell and Smith-Konter* [2017] model for topographic driven stress at seismogenic depth (5 km). Luttrell and Smith-Konter define a physics-based model constrained by gravity that assumes Cajon Pass topography to be built to a state of near critical failure. The model provides an estimate for stress tensor orientation and minimum magnitude

(L̇) Stress Accumulation Rate from Locked Fault Segments: *Burkhard et al.* [2018]

In this research we make use of the *Burkhard et al.* [2018] model for locked fault stress accumulation rate at Cajon Pass. *Burkhard et al.* [2018] employ a four-dimensional kinematic model, constrained by geodetic slip rates, for two-dimensional interseismic stress accumulation rates at half locking depths on SAF/SJF segments. The 2018 model is an update to the *Smith-Konter and Sandwell* [2009] estimate for locked fault stress accumulation rates that incorporates new lateral variations in crustal rigidity constrained by thermal parameters from regional thermal models. In comparison, this updated model produces 5-10% smaller stress accumulation rates on major Cajon Pass fault segments. To use this model in conjunction with models of stress from other tectonic sources we scale the accumulation rate estimates by incorporating effective loading times (t_{load}) on each fault segment to define the stress contribution from locked portions of the Cajon Pass crust.

(G) Stress from Geodynamic Plate Driving Forces

In this assessment we develop a set of simple driving stress models, in which we treat driving stress orientations (G_θ) and magnitudes (G_{dS}) as free parameters to populate far field stress tensors.

SCEC Community Fault Model

The Southern California Earthquake Center Community Fault Model v. 5.2 defines a three-dimensional representation of active faults across southern California. This model provides the triangulated surfaces and associated normal, strike, and dip vectors along major fault segments in the region [*Nicholson et al.*, 2017]. We adopt the geometries of five distinct segments (Mojave, San Bernardino, Mission Creek, Claremont, and Clark) at Cajon Pass to resolve stress fields onto

fault surfaces. We use this model to predict on fault estimates for stress (i.e. rake angle and shear stress) outlined in Appendix B.

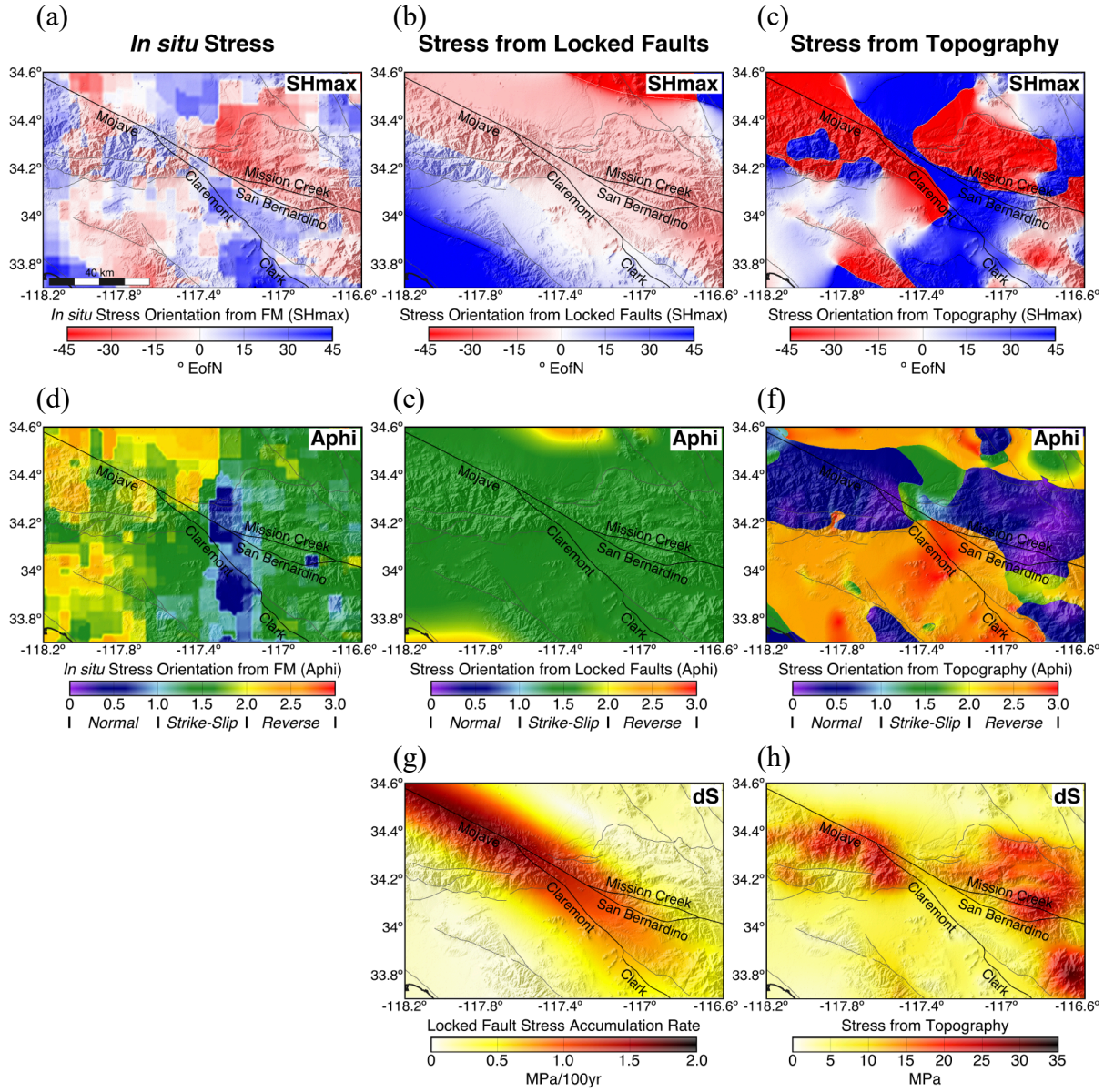

Figure A1. Visualization of stress from existing models; *In situ* stress from focal mechanisms [*Yang and Hauksson*, 2013]; stress accumulation along locked faults [*Burkhard et al.*, 2018]; and stress from topography [*Luttrell and Smith-Konter*, 2017]. (a,b,c) SHmax orientation of stress fields. (d,e,f) Aphi orientation of stress fields. (g) Stress accumulation rate due to loading of locked fault segments. (h) Magnitude of stress from topography.

Appendix B. Stress Metrics

The defined forward model is limited to available indications of stress from existing models. These models rely on unique methods to estimate stress orientation, magnitude, or both. While *Luttrell and Smith-Konter* [2017] and *Burkhard et al.* [2018] component models provide information on respective stress magnitudes and orientations, the *Yang and Hauksson* [2013] model for *in situ* stress at Cajon Pass solely carries stress orientation and shape estimates. To address this, we define set of stress metrics for stress tensor visualization and magnitude and orientation comparison. In this consideration of stress, negative and positive conventions correspond to compression and tension respectively, and thus principal stress magnitudes, σ_1, σ_2, σ_3, range from most tensional to most compressional. To indicate stress tensor magnitude, we refer to the differential stress, dS in MPa.

$$dS = \sigma_1 - \sigma_3 \quad \text{(Equation B1)}$$

To characterize stress tensor orientation completely it is helpful to divide orientation in two independent scalar 'shape' and 'azimuth' parameters, as in *Luttrell and Smith-Konter* [2017]. To describe stress tensor shape we adapt *Angelier's* [1979] stress ratio, R.

$$R = \frac{\sigma_2 - \sigma_1}{\sigma_3 - \sigma_1} \quad \text{(Equation B2)}$$

R compares the intermediate to the maximum and minimum principal stresses to convey relative magnitude information in a single quantity. This ratio does not consider which principal stress is most vertical, an indication of preferred faulting style [*Anderson*, 1905; 1951]. We adopt the more comprehensive Anderson fault parameter, A_{phi}, defined by *Simpson* [1997], to quantitatively compare tectonic regimes based on principal stresses.

$$A_{phi} = (n + 0.5) + (-1)^n (R - 0.5) \quad \text{(Equation B3)}$$

N equals 0, 1, or 2 for when respectively σ_1, σ_2, or σ_3 is most vertical. A_{phi} ranges continuously from 0-1 for normal, 1-2 for strike-slip, and 2-3 for reverse faulting regimes. Here we use the Anderson fault parameter to indicate the overall regime of the stress field. Neither the stress ratio nor the Anderson fault parameter conveys any indication of the horizontal azimuth of the stress field. We represent the azimuth of stress tensors by the direction of maximum compression, SHmax in ºEofN. Representation of stress tensor orientation by the azimuth of maximum horizontal compressive stress is common in stress field visualizations [*Hardebeck and Hauksson*, 2001; *Luttrell and Smith-Konter*, 2017; *Yang and Hauksson*, 2013]. We estimate SHmax orientations by the algorithm of *Lund and Townend* [2007], where V_{ni} corresponds to principal stress orientations.

$$SH_{max} = \frac{1}{2}\tan^{-1}\frac{2(V_{3y}V_{3x} + (1 - R)V_{2y}V_{2x})}{(V_{3y}^2 - V_{3x}^2) + (1 - R)(V_{2y}^2 - V_{2x}^2)} \quad \text{(Equation B4)}$$

Along with quantitatively describing a stress field it is useful to determine how stress might manifest on active fault segments. We use normal, $\hat{n}$, and strike, $\hat{s}$, unit vectors of over 5000 triangulated surfaces to resolve stress fields onto Cajon Pass fault surfaces. We predict maximum

shear stresses and rake angles of stress field on 3D surfaces to describe the on fault behavior of stress in this study. Shear stress and rake angle estimates are calculated according to *Fialko et al.* [2005] and *Aki and Richards* [2002]. We determine the total traction vector, T, of the stress tensor closest to the fault surface, S, by

$$T = \begin{bmatrix} S_{xx} & S_{xy} & S_{xz} \\ S_{xy} & S_{yy} & S_{yz} \\ S_{xz} & S_{yz} & S_{yy} \end{bmatrix} \begin{bmatrix} n_x \\ n_y \\ n_z \end{bmatrix} \quad \text{(Equation B5)}$$

We resolve the full traction vector into the normal stress component, Tn, by

$$Tn = T \cdot \hat{n} \quad \text{(Equation B6)}$$

The maximum shear stress vector, T_{mss}, is calculated by subtracting the normal traction vector from the total traction vector in Equation B7.

$$T_{mss} = T - T_n \cdot \hat{n} \quad \text{(Equation B7)}$$

Maximum shear stress, $|T_{mss}|$, is the magnitude of this vector, measured in MPa.

$$|T_{mss}| = \sqrt{T_{mss_x} + T_{mss_y} + T_{mss_z}} \quad \text{(Equation B8)}$$

The rake vector, $\hat{r}$, represents the unit vector of the maximum shear stress.

$$\hat{r} = \frac{T_{mss}}{|T_{mss}|} \quad \text{(Equation B9)}$$

We consider rake angle, in Equation B10, to be the angle between the rake and strike vectors, with the sign of the r_z component.

$$\text{rake} = \cos^{-1}(\hat{r} \cdot \hat{s}) \quad \text{(Equation B10)}$$

We determine rake angles in degrees, as defined by *Aki and Richards* [2002], ranging from -180 to 180º. We regard rake as the angle between the strike and predicted slip directions within the fault plane, and as such it can be used to predict preferred faulting behavior. Rake angles of ±180º, -90º, 0, and 90º indicate right lateral strike-slip, normal, left lateral strike-slip, and reverse faulting respectively.

Yang and Hauksson [2013] provide uncertainties in SHmax orientation for their stress estimate from the inversion of earthquake focal mechanisms. It is helpful to examine how a difference in SHmax orientation might present itself in rake angle calculated along Cajon Pass fault surfaces. In Figure B1 we plot the effect of change in SHmax orientation for the *Yang and Hauksson* [2013] stress field on average rake angle predicted along Cajon Pass fault segments.

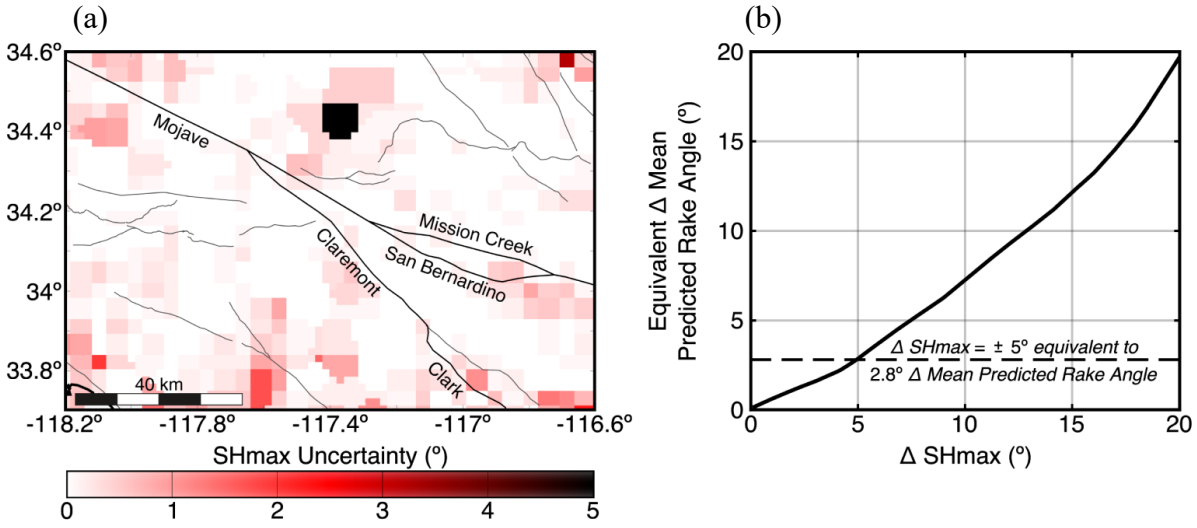

Figure B1. Effect of change in SHmax orientation on average predicted rake angle along Cajon Pass fault surfaces (a) Map of uncertainty in SHmax orientation for the *Yang and Hauksson* [2013] stress estimate. (b) Change in rake angle predicted on Cajon Pass fault surfaces for the *Yang and Hauksson* [2013] field if SHmax orientations were to vary by some value.

Appendix C. Previous Methods

Models were previously assessed on their ability to recreate local heterogeneities in SHmax and Aphi in the focal mechanism stress estimate. To compare the three-dimensional orientations of stress fields we used the scalar misfit parameter, E, defined by *Luttrell and Smith-Konter* [2017]. E between two arbitrary stress fields A and B is defined as

$$E\langle A|B\rangle = 1 - \frac{A' : B'}{\sqrt{A' : A'}\sqrt{B' : B'}} \qquad \text{(Equation C1)}$$

where A' represent the deviatoric component of A, and the colon operator signifies the tensor scalar dot product. Scalar misfit ranges continuously from 0-2, where E=0 indicates all three principal axes of A and B in perfect alignment, and E=2 indicates perfect misalignment. As stress fields in general vary spatially, we considered the mean scalar misfit over each fault segment to designate a single quantity to model fit. Low mean scalar misfit corresponded to better fitting models. As E captures the full 3D orientation differences between two tensors, it is helpful to examine how a difference in orientation by only the horizontal azimuth ($\Delta\theta$) might present itself in E (Figure C1).

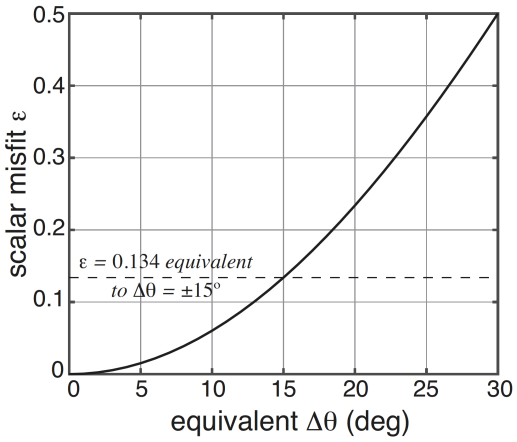

Figure C1. Scalar misfit for two stress fields whose orientations differ only in azimuth (i.e. equal A_{phi} values, different SHmax values). Figure from *Luttrell and Smith-Konter* [2017].

Below are the results from our interrogation with scalar misfit, E, as the model fit parameter.

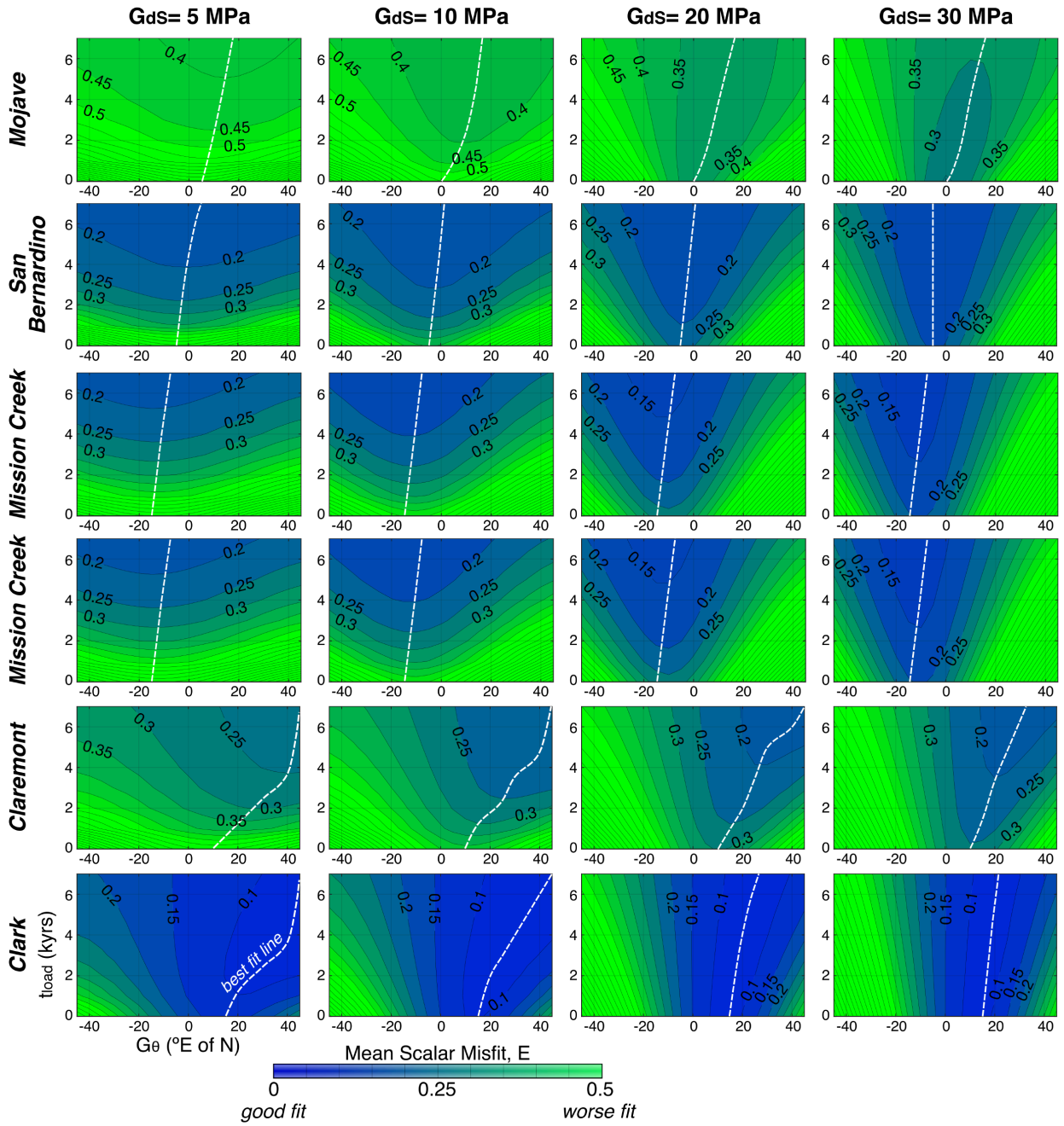

Figure C2. Complete parameter space on all five fault segments. Contours of mean scalar misfit on each fault segment between stress estimates from focal mechanisms and forward models for a set of driving stress magnitudes (G_{dS}), orientations (G_{θ}), and loading times (t_{load}) on locked fault segments. Best fit lines (white dashed) represent driving stress orientations and locked fault loading times that best fit rake estimates from the focal mechanism estimate.

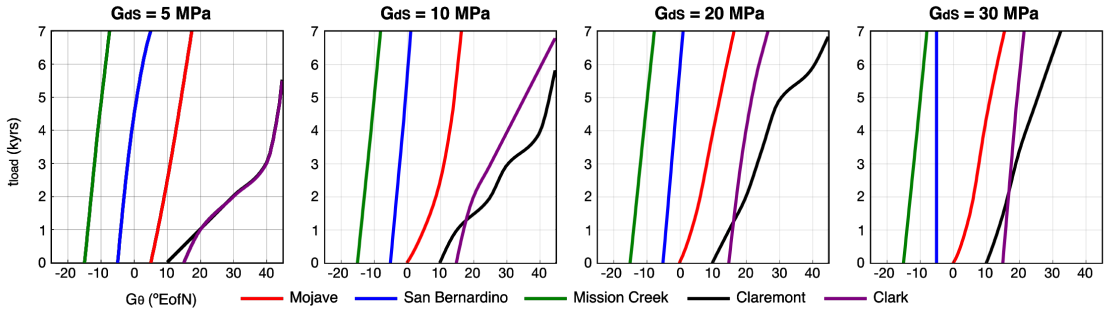

Figure C3. Best fit lines. Lines of driving stress orientations and loading times for each fault segment that best fit focal mechanism rake angles with a driving stress of 5; 10; 20; and 30 MPa. White dashed lines in Figure C2.

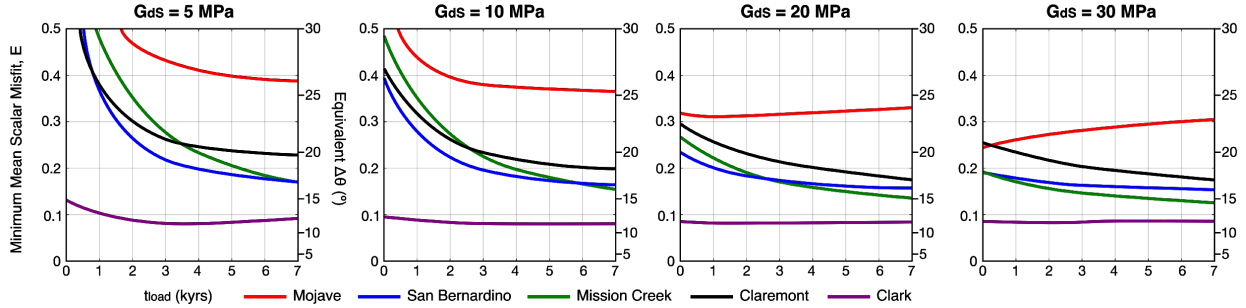

Figure C4. Effect of driving stress magnitude on model fit (all segments together). Lines of minimum mean scalar misfit for best fitting load times on each fault segment with a driving stress of 5; 10; 20; and 30 MPa.

E is most sensitive to changes in the relative orientation of principal stresses between two stress fields. We find that it is possible for stress tensors with large scalar misfit to alternately predict similar on fault behaviors (i.e. rake angle; normal stress; shear stress) when resolved onto fault surfaces (Figure C5). As we are primarily concerned with the manifestation of stress on major fault segments in the Cajon Pass area, we find that scalar misfit may not be the best metric of comparison between stress fields. When we use absolute rake angle difference to define model fit, we are able to better fit the focal mechanism stress estimate than when we use the scalar misfit parameter to assess model fit (Figure C5). For these reasons we use rake angle difference as the primary criteria to appraise model fit.

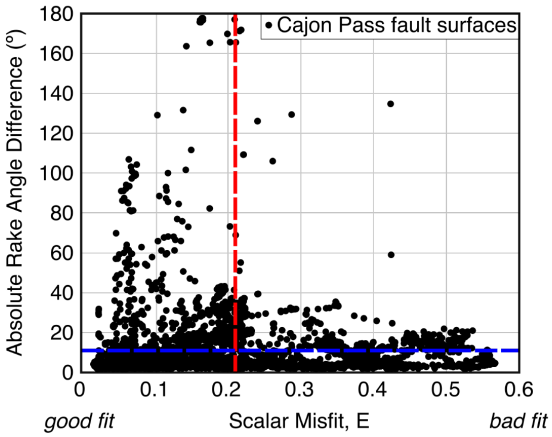

Figure C5. Comparison of model fit parameters. Plot of absolute rake angle difference and scalar misfit on Cajon Pass fault surfaces between the focal mechanism estimate and a forward model with paleoseismic loading times (Table 2) and a 30 MPa driving stress with compression oriented north-south. Dashed lines denote the mean scalar misfit (red) and mean absolute rake angle difference (blue) for this model.

Appendix D. Supplemental Figures

Included in this appendix are a complete list of figures referenced in this document. Portions of these figures may appear in earlier sections.

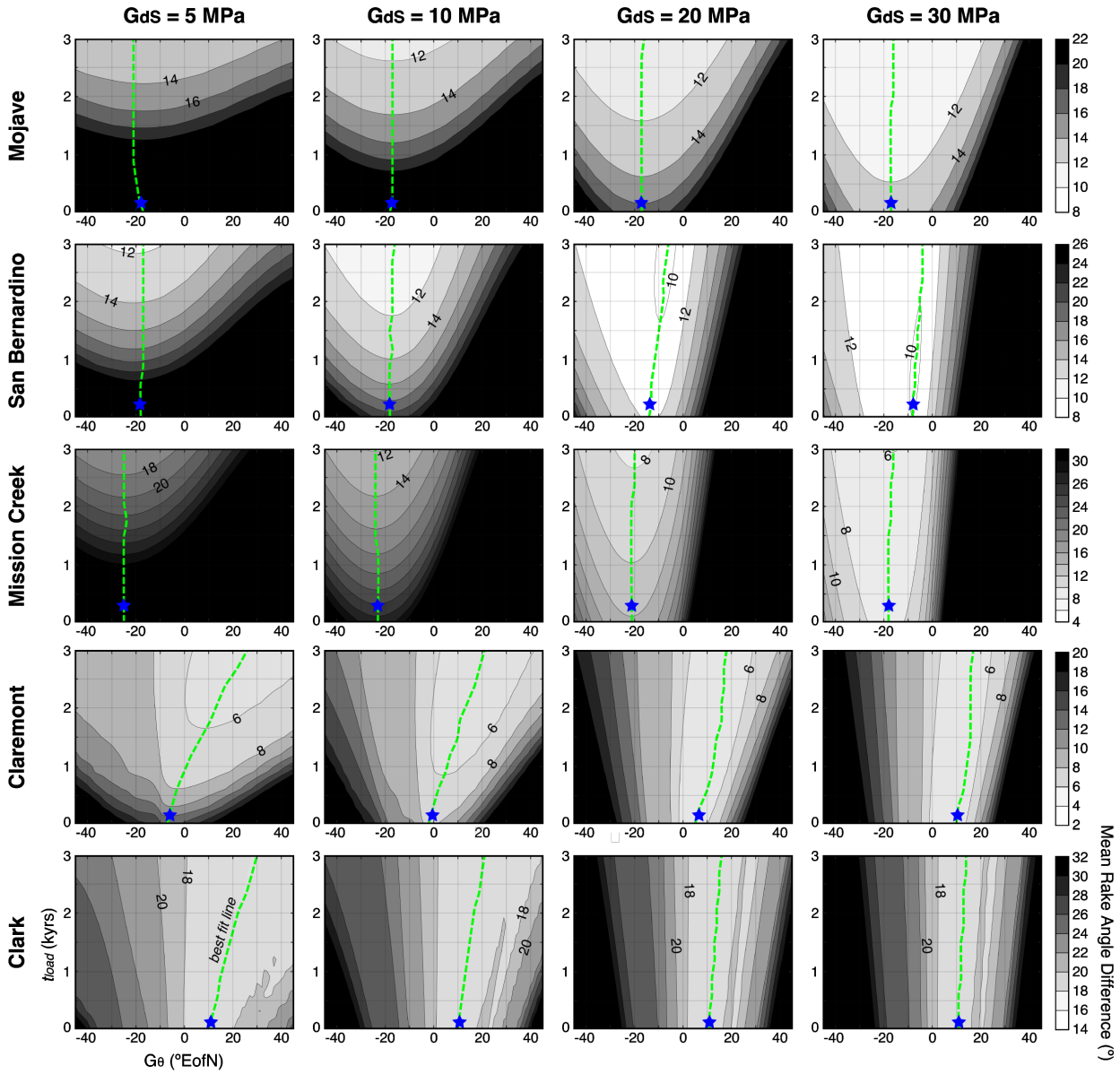

Figure D1. Model fit across complete parameter space for all five fault segments. 2º Contours of mean predicted rake angle difference between stress estimates from focal mechanisms and forward models with variable driving stress magnitudes (G_{dS}), orientations (G_{θ}), and loading times (t_{load}) on locked fault segments. Best fit lines (green dashed) indicate driving stress orientations that minimize misfit at each locked fault loading time. Stars indicate time since last rupture on respective segments [*T K Rockwell et al.*, 2015; *R Weldon et al.*, 2004]. Note that color scales change between fault segments.

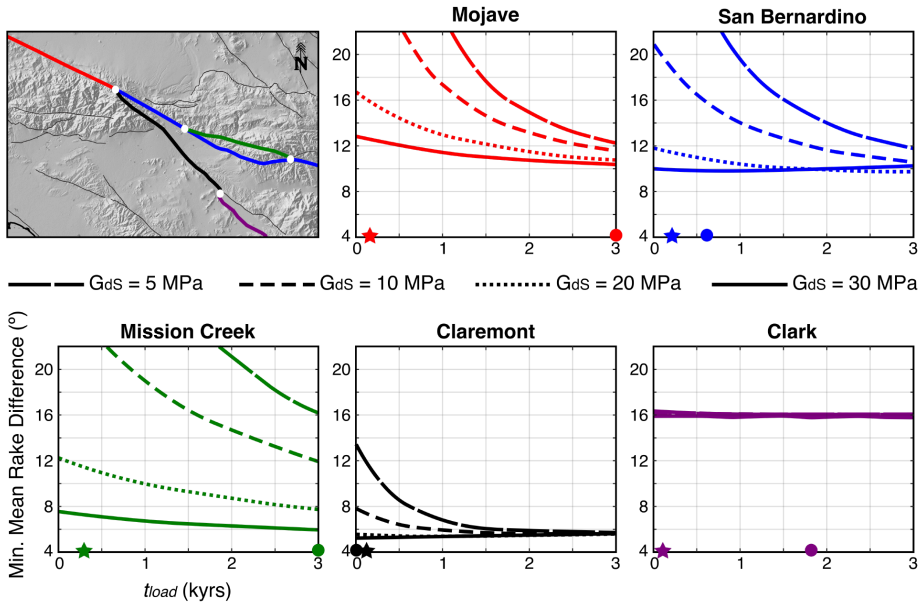

Figure D2. Effect of driving stress magnitude on model fit (each segment individually). Minimum mean rake angle difference as a function of load times on all fault segments, using different driving stress magnitudes as indicated. Stars indicate the time since last rupture on each fault segment [*T K Rockwell et al.*, 2015; *R Weldon et al.*, 2004] , and circles represent the loading time that produces the absolute best fit for each fault segment (Table 3a).

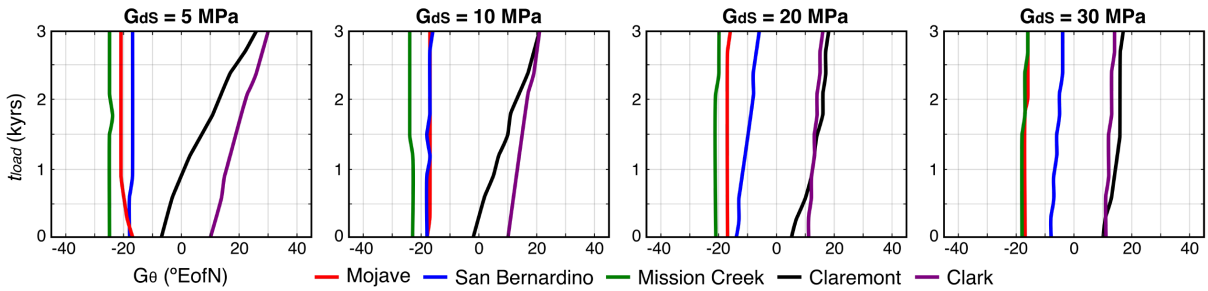

Figure D3. Best fit lines. Lines of best fitting G_θ and t_{load} on all fault segments using different driving stress magnitudes as indicated. Green dashed lines in Figure D1.

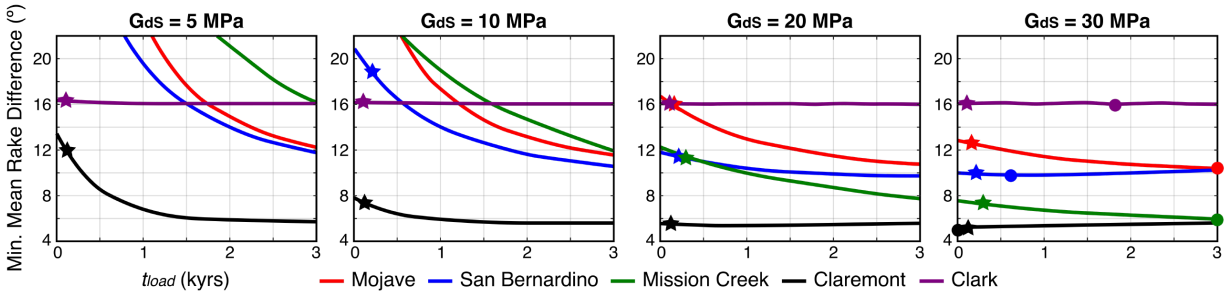

Figure D4. Effect of driving stress magnitude on model fit (all segments together). Stars indicate the time since last rupture on each fault segment [*T K Rockwell et al.*, 2015; *R Weldon et al.*, 2004], and circles represent the loading time that produces the absolute best fit for each fault segment (Table 3a).

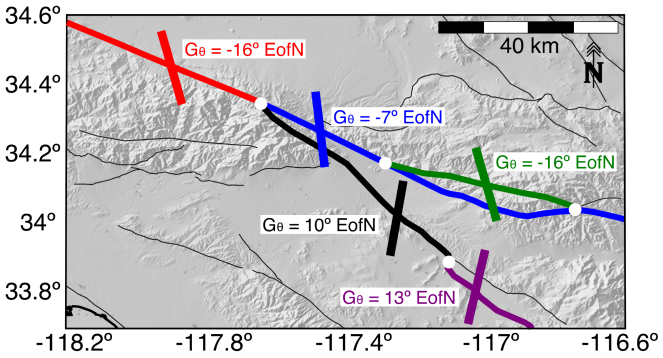

Figure D5. Visualization of best fitting driving stress orientations. Bold bars denote the orientation of principal compression for each driving stress necessary to maximize fit to focal mechanism rake angles on each fault segment (Table 3a). We observe a clockwise rotation in driving stress azimuth (from north-northwest to north-northeast) southward across the Cajon Pass region.

References

Aki, K., and P. G. Richards (2002), *Quantitative Seismology*, 2 ed., University Science Books.

Albright, L. B. (1999), Magnetostratigraphy and biochronology of the San Timoteo Badlands, southern California, with implications for local Pliocene-Pleistocene tectonic and depositional patterns, *Geological Society of America Bulletin*, *111*, 1265-1293.

Anderson, E. M. (1905), The dynamics of faulting, *Transactions of the Edinburgh Geological Society 8*, 387-402.

Anderson, E. M. (1951), The Dynamics of Faulting and Dyke Formation With Applications to Britain, *Transactions of the Edinburgh Geological Society*, 206.

Angelier, J. (1979), Determination of the mean principal directions of stresses for a given fault population, *Tectonophysics*, *56*, 17-26.

Becker, T. W., J. L. Hardebeck, and G. Anderson (2005), Constraints on fault slip rates of the southern California plate boundary from GPS velocity and stress inversions, *Geophysical Journal International*, *160*, 634-650.

Bennett, R. A., A. M. Friedrich, and K. P. Furlong (2004), Codependent histories of the San Andreas and San Jacinto fault zones from inversion of fault displacement rates, *Geology 32*, 961-964.

Bennett, R. A., W. Rodi, and R. E. Reilinger (1996), GPS constraints on fault slip rates in southern California and northern Baja, Mexico, *Journal of Geophysical Research*, *101*, 21943-21960.

Brune, J. N., T. L. Henyey, and R. F. Roy (1969), Heat flow, stress, and rate of slip along the San Andreas fault, California, *Journal of Geophysical Research*, *74*, 3821-3827.

Burkhard, L., B. Smith-Konter, L. Ward, K. Scharer, and D. Sandwell (2018), Earthquake cycle stress accumulation disparities of the Cajon Pass region, *Poster Presentation at 2018 SCEC Annual Meeting*, 262.

Dorsey, R. J. (2002), Stratigraphic record of Pleistocene initiation and slip on the Coyote Creek fault, lower Coyote Creek, southern California, *Geological Society of America Special Paper*, *365*, 251-269.

Fialko, Y., L. Rivera, and H. Kanamori (2005), Estimate of differential stress in the upper crust from variations in topography and strike along the San Andreas fault, *Geophysical Journal International*, *160*, 527-532.

Frizzle, V. A., J. M. Mattinson, and J. C. Matti (1986), Distinctive Triassic megaporphyritic monzogranite: Evidence for only 160 km offset along the San Andreas fault, southern California, *Journal of Geophysical Research*, *91*, 14080=14088.

Fumal, T. E., D. P. Schwartz, S. K. Pezzopane, and R. J. Weldon (1993), A 100-Year Average Recurrence Interval for the San Andreas Fault at Wrightwood, California, *Science*, *259*, 199-203.

Ghosh, A., and W. E. Holt (2012), Plate Motions and Stresses from Global Dynamic Models, *Science*, *335*, 838-842.

Goebel, T. H. W., E. Hauksson, P. M. Shearer, and J. P. Ampuero (2015), Stress-drop heterogeneity within tectonically complex regions: a case study of San Gorgonio Pass, southern California, *Geophysical Journal International*, *202*, 514-528.

Grant, L. B., and W. R. Lettis (2002), Introduction to the special issue on paleoseismology of the San Andreas fault system, *Bulletin of the Seismological Society of America*, *92*, 2552-2554.

Grant-Ludwig, L., J. N. Brune, A. Anooshehpoor, M. D. Purvance, R. J. Brune, and J. C. Lozos (2015), Reconciling precariously balanced rocks (PBRs) with large earthquakes on the San Andreas fault system, *Seismological Research Letters*, *86*, 1345-1353.

Hardebeck, J. L., and E. Hauksson (2001), Crustal stress field in southern California and its implications for fault mechanics, *Journal of Geophysical Research*, *106*, 21859-21882.

Hardebeck, J. L., and A. J. Michael (2006), Damped regional-scale stress inversions: Methodology and examples for southern California and the Coalinga aftershock sequence, *Journal of Geophysical Research*, *111*.

Harden, J. W., and J. C. Matti (1989), Holocene and late Pleistocene slip rates on the San Andreas fault in Yucaipa, California, using displaced alluvial-fan deposits and soil chronology, *Geological Society of America Bulletin*, *101*, 1107-1117.

Harris, R. A., et al. (2018), A Suite of Exercises for Verifying Dynamic Earthquake Rupture Codes, *Seismological Research Letters*, *89*, 1146-1162.

Hartog, R., and S. Y. Schwartz (2001), Depth-dependent Mantle Anisotropy below the San Andreas Fault System: Apparent Splitting Parameters and Waveforms, *Journal of Geophysical Research*, *106*, 4155-4167.

Hauksson, E. (2015), Average Stress Drops of Southern California Earthquakes in the Context of Crustal Geophysics: Implications for Fault Zone Healing, *Pure and Applied Geophysics*, *172*, 1359-1370.

Lachenbruch, A. H., and J. H. Sass (1980), Heat Flow and Energetics of the San Andreas Fault Zone, *Journal of Geophysical Research*, *85*, 6185-6222.

Li, Q., and M. Liu (2007), Initiation of the San Jacinto Fault and its Interaction with the San Andreas Fault: Insights from Geodynamic Modeling, *Pure and Applied Geophysics*, *164*, 1937-1945.

Lisowski, M., J. C. Savage, and W. H. Prescott (1991), The Velocity Field Along the San Andreas Fault in Central and Southern California, *Journal of Geophysical Research*, *96*, 8369-8389.

Lozos, J. C. (2016), A case for historic joint rupture of the San Andreas and San Jacinto faults, *Science Advances*, *2*.

Lozos, J. C., D. D. Oglesby, J. N. Brune, and K. B. Olsen (2015), Rupture and Ground-Motion Models on the North San Jacinto Fault, Incorporating Realistic Complexity, *Bulletin of the Seismological Society of America*, *105*, 1931-1946.

Lund, B., and J. Townend (2007), Calculating horizontal stress orientations with full or partial knowledge of the tectonic shear tensor, *Geophysical Journal International*, *170*, 1328-1335.

Luttrell, K., and B. Smith-Konter (2017), Limits on crustal differential stress in southern California from topography and earthquake focal mechanisms, *Geophysical Journal International*, *211*, 472-482.

Magistrale, H., S. Day, R. W. Clayton, and R. Graves (2000), The SCEC Southern California Reference Three-Dimensional Seismic Velocity Model Version 2, *Bulletin of the Seismology Society of America*, *90*, S65-S76.

Matti, J. C., and D. M. Morton (1993), Paleogeographic evolution of the San Andreas fault in southern California: A reconstruction based on a new cross fault correlation. In the San Andreas Fault System: Displacement, Palinspastic Reconstruction, and Geologic Evolution (R.E. Powell et al. ed.), *Geological Society of America Memoir*, 107-159.

Meade, B. J., and B. H. Hager (2005), Block models of crustal deformation in southern California constrained by GPS measurements, *Journal of Geophysical Research*, *110*, B03403.

Mount, V. S., and J. Suppe (1987), State of stress near the San Andreas fault: Implications for wrench tectonics, *Geology*, *15*, 1143-1146.

Nicholson, C., A. Plesch, and J. H. Shaw (2017), Community Fault Model Version 5.2: Updating & expanding the CFM 3D fault set and its associated fault database, *Poster Presentation at 2017 SCEC Annual Meeting*, SCEC Contribution 7735.

Onderdonk, N. W., S. F. McGill, and T. K. Rockwell (2015), Short-term variations in slip rate and size of prehistoric earthquakes during the past 2000 years on the northern San Jacinto fault zone, a major plate-boundary structure in southern California, *Lithosphere*, *7*(3), 211-234.

Powell, R. E., and R. J. Weldon (1992), Evolution of the San Andreas fault, *Annual Reviews of Earth and Planetary Science*, *20*, 431-468.

Rockwell, T., C. Loughman, and P. Marifield (1990), Late Quaternary rate of slip along the San Jacinto fault zone near Anza, southern California, *Journal of Geophysical Research*, *95*, 8593-8605.

Rockwell, T. K., T. E. Dawson, J. Y. Ben-Horin, and G. Seitz (2015), A 21-Event, 4,000-Year History of Surface Ruptures in the Anza Seismic Gap, San Jacinto Fault, and Implications for Long-term Earthquake Production on a Major Plate Boundary Fault, *Pure and Applied Geophysics*, *172*, 1143-1165.

Shamir, G., and M. D. Zoback (1992), Stress Orientation Profile to 3.5 km Depth Near the San Andreas Fault at Cajon Pass, California, *Journal of Geophysical Research*, *97*, 5059-5080.

Sharp, R. V. (1967), San Jacinto fault zone in the Peninsular Ranges of southern California, *Geological Society of America Bulletin*, *78*, 705-730.

Sharp, R. V. (1981), Variable rates of late Quaternary strike-slip on the San Jacinto fault zone, southern California, *Journal of Geophysical Research*, *86*, 1754-1762.

Silver, L. T., and E. W. James (1988), Geologic Setting and Lithologic Column of the Cajon Pass Deep Drillhole, *Geophysical Research Letters*, *15*, 941-944.

Simpson, R. W. (1997), Quantifying Anderson's fault types, *Journal of Geophysical Research*, *102*, 17909-17919.

Smith, B., and D. Sandwell (2003), Coulomb stress accumulation along the San Andreas Fault system, *Journal of Geophysical Research*, *108*(6), 3-17.

Smith-Konter, B., and D. T. Sandwell (2009), Stress evolution of the San Andreas Fault System: Reccurence intervals versus locking depth, *Geophysical Research Letters*, *36*.

Swanson, M. T. (2005), Geometry and kinematics of adhesive wear in brittle strike-slip fault zones, *Journal of Structural Geology*, *27*, 871-887.

Tong, X., D. T. Sandwell, and B. Smith-Konter (2013), High-resolution interseismic velocity data along the San Andreas Fault from GPS and InSAR, *Journal of Geophysical Research*, *118*, 369-389.

Van Der Woerd, J., Y. Klinger, K. Sieh, P. Tapponnier, F. J. Ryerson, and A. S. Mériaux (2006), Long-term slip rate of the southern San Andreas fault from 10Be-26Al surface exposure dating of an offset alluvial fan, *Journal of Geophysical Research*, *111*.

Vernik, L., and M. D. Zoback (1989), Effects of Rock Elastic and Strength Properties in Estimation of the State of Stress at Depth, *International Society for Rock Mechanics and Rock Engineering*, 1033-1040.

Vernik, L., and M. D. Zoback (1992), Estimation of Maximum Horizontal Principal Stress Magnitude From Stress-Induced Well Bore Breakouts in the Cajon Pass Scientific Research Borehole, *Journal of Geophysical Research*, *97*, 5109-5119.

Weldon, R., T. Fumal, G. Biasi, and K. Scharer (2005), Past and future earthquake on the San Andreas fault, *Science*, *308*, 966-967.

Weldon, R., K. Scharer, T. Fumal, and G. Biasi (2004), Wrightwood and the earthquake cycle: What a long recurrence records tells us about how fault work, *Geological Society of America*, *14*, 4-10.

Weldon, R. J., and K. E. Sieh (1985), Holocene rate of slip and tentative recurrence interval for large earthquakes on the San Andreas fault, Cajon Pass, southern California, *Geological Society of America Bulletin*, *96*, 793-812.

Yang, W., and E. Hauksson (2013), The tectonic crustal stress field and style of faulting along the Pacific North American Plate boundary in Southern California, *Geophysical Journal International*, *194*.

Yang, W., E. Hauksson, and P. M. Shearer (2012), Computing a Large Refined Catalog of Focal Mechanisms for Southern California (1981-2010): Temporal Stability and Style of Faulting, *Bulletin of the Seismological Society of America*, *102*, 1179-1194.

Zoback, M. D., and J. H. Healy (1992), In Situ Stress Measurements to 3.5 km Depth in the Cajon Pass Scientific Research Borehole: Implications for the Mechanics of Crustal Faulting, *Journal of Geophysical Research*, *97*, 5039-5057.

Zoback, M. D., S. Hickman, and W. Ellsworth (2010), Scientific Drilling Into the San Andreas Fault Zones, *Eos Transactions American Geophysical Union*, *91*, 197-199.

Vita

Elliott Conley Helgans, born in Darien, Connecticut, was fascinated with the physical sciences from a young age. At Washington and Lee University, where he earned his bachelor's degree, this attraction took shape. He ultimately decided to further his interest by enrolling in the Geology and Geophysics Department at Louisiana State University. Upon completion of his master's degree he will begin work in the Oil and Gas industry.